Key Genetic Determinants Driving Esophageal Squamous Cell Carcinoma Initiation and Immune Evasion

Kyung-Pil Ko,[1] Yuanjian Huang,[1] Shengzhe Zhang,[1] Gengyi Zou,[1] Bongjun Kim,[1] Jie Zhang,[1] Sohee Jun,[1] Cecilia Martin,[2] Karen J. Dunbar,[2] Gizem Efe,[2] Anil K. Rustgi,[2] Hiroshi Nakagawa,[2] Jae-Il Park[1,3,4,*]

[1]Department of Experimental Radiation Oncology, Division of Radiation Oncology, The University of Texas MD Anderson Cancer Center, Houston, TX 77030, USA

[2]Division of Digestive and Liver Diseases, Department of Medicine, Herbert Irving Comprehensive Cancer Center, Columbia University Irving Medical Center, New York, NY 10032, USA

[3]The University of Texas MD Anderson Cancer Center UTHealth Houston Graduate School of Biomedical Sciences, Houston, TX 77030, USA

[4]Program in Genetics and Epigenetics, The University of Texas MD Anderson Cancer Center, Houston, TX 77030, USA

*Correspondence: Jae-Il Park
E-mail: jaeil@mdanderson.org; Tel: 713-792-3659; Fax: 713-794-5369
Keywords: Esophageal squamous cell cancer, CCL2, CCR2, organoids, esophageal neoplasia, immune evasion, single-cell RNA-sequencing

Abstract

Despite recent progress in identifying aberrant genetic and epigenetic alterations in esophageal squamous cell carcinoma (ESCC), the mechanism of ESCC initiation remain unknown. Using genetically engineered esophageal organoids (EOs), we identified the key genetic determinants that drive ESCC tumorigenesis. A single-cell transcriptomic analysis uncovered that *Trp53*, *Cdkn2a*, and *Notch1* (PCN) triple knockout (KO) induces neoplastic features of ESCC by generating distinct cell lineage trajectories with multiple root cells and high cell plasticity. Although *Trp53* and *Notch1* (PN) double KO was sufficient to induce esophageal neoplasia and cellular heterogeneity, additional inactivation of *Cdkn2a* was indispensable for immune landscape remodeling for *in vivo* tumorigenesis. *PCN* KO generated immunosuppressive niche enriched with exhausted T cells and M2 macrophages via the CCL2-CCR2 axis in an autochthonous ESCC mouse model. Moreover, genetic or pharmacological blockade of the CCL2-CCR2 axis suppressed ESCC tumorigenesis. Comparative single-cell transcriptomic analyses classified ESCC patient tumors into three subgroups and identified a specific subset recapitulating PCN-type ESCC signatures, including the high expression of CCL2 and CD274/PD-L1. Our study unveils that loss of *TP53*, *CDKN2A*, and *NOTCH1* induces esophageal neoplasia and immune evasion for ESCC initiation and proposes the CCL2 blockade as a viable approach to target a subset of ESCC.

Introduction

Esophageal squamous cell carcinoma (ESCC) accounts for over 80% of all cases of esophageal cancer and has a poor prognosis because of a lack of symptoms in the early stages. The 5-year overall survival rate of patients with esophageal cancer ranges from 10% to 25%[1]. ESCC develops from squamous dysplasia as a typical invasive histologic precursor lesion[2], which makes it difficult to detect early and leads to late detection. Therefore, understanding the mechanisms of esophageal neoplasia and ESCC initiation is imperative to improve the detection, diagnosis, treatment, and prevention of ESCC. However, despite a recent genome-wide analysis of ESCC patients, the key genetic factors that drive ESCC neoplasia and initiation remain elusive.

In addition to the genetic and epigenetic alteration of tumor cells, the tumor microenvironment (TME) plays a pivotal role in tumorigenesis. The TME comprises immune and stromal cells surrounding tumor cells and is known to design the immune landscape to elicit immunosuppressive effects on tumors and various immunotherapeutic responses[3,4]. Although the TME's effects on tumor cells are biphasic, as immune cells generally recognize tumor cells or neoantigens to generate anti-tumor immune responses[5], the tumor-favorable TME induces tumor growth, invasion, and metastasis[6]. The TME is also regarded as an indispensable factor in ESCC development, as it provides drug resistance and immunosuppressive immune cell infiltration[7,8].

Immune cell profiling using single-cell transcriptomics has been used to elucidate the immune landscape of ESCC patients[9-11]. An immunosuppressive tumor niche is frequently observed in these patients, and immunotherapy is expected to be effective based on immune cell profiling results. Indeed, immune checkpoint inhibitors (ICIs) have been clinically tested in ESCC patients and have shown some promising results[12-16]. However, not all patients benefit from ICIs alone or combined with first-line therapy[7], possibly because of the lack of a clear classification of ESCC patients. The underlying genetic background or biomarkers in ICIs responders and non-responders have yet to be identified. Therefore, in this study, we sought to determine key genetic events driving ESCC initiation and generating tumor-favorable immune environments.

Results

Genetic ablation of *Trp53* and *Notch1* is sufficient to induce esophageal neoplasia

To elucidate the vital genetic events initiating ESCC, we analyzed genetic alterations in ESCC patients (n = 86). Recurrent loss-of-function mutations in the *TP53*, *CDKN2A*, *KMT2D*, *KMT2C*, *FAT1*, *FAT4*, *AJUBA*, *NOTCH1*, and *NOTCH3* genes were observed in ESCC patients, consistent with previous studies[17,18]. Genetic alterations of the nine genes frequently co-occurred, and the *TP53* and *CDKN2A* genes were the most commonly altered (> 70%) (Extended Data 1a). More than 50% of mutations in the *CDKN2A*, *KMT2D*, *NOTCH1*, and *FAT1* genes were frameshift or truncation mutations (Extended Data 1b). Also, ESCC patients displayed transcriptional downregulation of *KMT2C* and *FAT4* genes (Extended Data 1c). These results imply that genetic inactivation of the *TP53*, *CDKN2A*, *KMT2D*, *KMT2C*, *NOTCH1*, *NOTCH3*, *FAT1*, *FAT4*, and *AJUBA* genes might be associated with ESCC tumorigenesis.

To understand significance of the nine genes in ESCC initiation, we tested functional impact of their inactivation on transformation of murine esophageal organoids (EOs), as we recently established[19] (Fig. 1a and Supplementary Fig. 1a). Employing the CRISPR gene editing system, we genetically ablated the nine genes in 32 different combinations. Given that the *TP53* and *CDKN2A* genes were the most frequently mutated in patients, *Trp53* KO and *Cdkn2a* KO were chosen as the foundation for additional gene ablations, and double KO (dKO) or triple KO (tKO) EOs were established (Extended Data 1d). Gene KO was confirmed by immunoblot and genomic DNA sequencing (Supplementary Fig. 1b, c). Next, we assessed the size, morphology, and differentiation of 32 genetically engineered EOs (O1-O32) (Extended Data 1e, f).

Intriguingly, in combination with *Trp53* and *Cdkn2a* dKO, KO of *Notch1*, *Fat4*, or *Ajuba* led to a markedly increased EO size (Fig. 1b). However, only *Notch1* KO with *Trp53* and *Cdkn2a* dKO EOs displayed a loss of cell differentiation and hyperplastic growth (Fig. 1c). The increased number of proliferating cells was confirmed by Mki67 staining in dKO of *Trp53* and *Notch1* (PN) and tKO of *Trp53*, *Cdkn2a*, and *Notch1* (PCN) EOs (Fig. 1d, e and Extended Data 2a). Sox2 and Trp63, markers for ESCC stemness, were also highly expressed in PN and PCN compared to other EOs (Fig. 1d, f and Extended Data 2a). A bromodeoxyuridine (BrdU) incorporation assay confirmed the increased cell proliferation in PN and PCN EOs (Figs. 1g, h). *Notch1* KO suppressed organoid cell differentiation, as represented by decreased Krt13, a cell differentiation marker (Fig. 1f and Extended Data 1b), and this effect was validated using DAPT, a Notch signaling inhibitor (Extended Data Figs. 2c, d).

Since ESCC invades the stromal cell layers at an early stage[20], we analyzed the cell invasiveness of EOs by co-culturing them on the stromal cell layer (Extended Data 2e). While WT EO-derived epithelial cells formed distinct epithelial cell colonies, PN and PCN EO-derived cells were mixed with the stromal cell layer (Fig. 1i, j), recapitulating the invasive feature of ESCC. We further examined the tumorigenicity of each group of EOs in the 2D-culture system to assess cell-autonomous growth without the supporting materials and growth factors included in the organoid culture system. In 2D-culture, only PN and PCN EOs showed colony formation and exponential cell growth, while other EOs failed to grow. Of note, PN EOs showed relatively faster growth than PCN EOs (Figs. 1k, l and Extended Data 2f). PN and PCN cells also displayed slightly increased

107 cell migration compared to 2D-cultured PC cells (Extended Data 2g). Of note, PN and PCN EOs
108 were not related to EAC (Extended Data 2h). These results suggest that *Trp53* and *Notch1* dKO
109 (PN) and *Trp53*, *Cdkn2a, Notch1* tKO (PCN) are sufficient to induce neoplastic transformation
110 exhibiting the characteristics of early-stage ESCC.

111 **Dysregulated cell plasticity and lineage trajectories of neoplastic EOs**

112 We next sought to understand the mechanism of ESCC initiation by single-cell transcriptomic
113 analysis. We performed single-cell RNA-sequencing (scRNA-seq) of WT, PC, PN, and PCN EOs.
114 Each library was sequenced with the multiplexing workflow, and the results were integrated using
115 sctransform (R) or Harmony (Python) (Fig. 2a-c and Extended Data 3a). Thirty-five cell clusters
116 were annotated with multiple markers that were specifically expressed in proliferative (Mki67,
117 Top2a, and Stmn1 markers), early suprabasal (Ptma, Itgb4, and Krt5 markers), intermediate
118 suprabasal (Itga6 marker), and stratified (Krt13, Krt4, and Sprr3 markers) cell types[19,21] (Extended
119 Data 3b-d). The intermediate suprabasal cell cluster showed a moderate expression level of early
120 suprabasal markers (Itgb4 and Krt5) and stratified markers. A cell proportion analysis showed that
121 the proliferative cells were significantly enriched in the PC, PN, and PCN organoids compared to
122 the WT EOs enriched with differentiated (stratified and suprabasal) cells (Fig. 2d and Extended
123 Data 3e). These results were consistent with the hyperproliferative phenotypes of PN or PCN EOs
124 (Fig. 1).

125 Having observed distinct cell hyperproliferation and de-differentiation by PN and PCN, we
126 examined the PN or PCN-specific cell lineages through RNA velocity–based cell trajectory
127 inferences with re-clustered UMAP projections (Fig. 2e). The cell lineages, indicated by a line of
128 arrows, show that PN and PCN have multiple root cell clusters, while WT and PC have a single
129 root cell cluster (Fig. 2f). Cell lineage trajectories were also assessed by the latent time and PAGA
130 analysis (Fig. 2g-i). The PAGA analysis visualized that PN and PCN harbored three root cell
131 clusters (PN3, PN4, and PN8 and PCN3, PCN4, and PCN7, respectively), while WT showed one
132 root cell cluster (WT4) (Fig. 2h, i), consistent with the RNA velocity results (Fig. 2f). Notably, PC
133 displayed two root cell clusters (PC4 and PC5) with relatively more straightforward lineage
134 trajectories than those of PN and PCN (Fig. 2h, i). These results suggest that the combined ablation
135 of *Trp53* and *Notch1* generates distinct cell plasticity and higher cellular heterogeneity, as shown
136 in malignant tumors[22].

137 **Human ESCC features in *Trp53* / *Notch1* dKO and *Trp53* / *Cdkn2a* / *Notch1* tKO EOs**

138 We assessed the pathological relevance of genetically engineered EOs to human ESCC by
139 comparing the transcriptional signatures of EOs with those of ESCC patients. Compared to WT
140 and PC EOs, ESCC cancer stem cell markers, including Trp63, Krt5, and Tfrc, were intensively
141 enriched in the proliferating cells of PN and PCN EOs (Fig. 3a). Sox2 and Gnl3 were highly
142 expressed in the proliferating cells of PN and PCN EOs, respectively, while the other genes did
143 not show the specificity to the PN or PCN cell types. We also compared the transcriptional features
144 of our EOs with those of ESCC patients from the TCGA database using the Scissor package. The
145 gene expression feature comparison analysis showed the similarity of each EO to ESCC patients:
146 WT (35.4%), PC (52.2%), PN (50.5%), and PCN (52.2%) (Fig. 3b, c). Additionally, PCN (21.9%)

147 showed the highest similarity with the poor survival–associated ESCC patients compared to the
148 other organoids (Fig. 3d, e). A gene set enrichment analysis further confirmed that the PCN highly
149 expressed gene set was enriched in ESCC-specific gene features, while the PN highly expressed
150 gene set enrichment was not statistically significant (Fig. 3f). To increase the depth of the
151 sequencing read, we also performed bulk RNA-seq of WT, PN, and PCN EOs and reanalyzed the
152 gene expression of each dataset (Fig. 3g). Using the differentially expressed genes (DEGs) of PN
153 to WT or PCN to WT, we ran the Enrichr analysis with PN or PCN highly expressed genes. Both
154 PN and PCN highly expressed genes were shown to be enriched with features of the cell cycle,
155 DNA replication, and mitotic cells in the Bioplanet and REACTOME databases (Fig. 3h). The
156 "pathways in cancer" were also associated with the PCN highly expressed genes in the Kyoto
157 Encyclopedia of Genes and Genomes (KEGG) pathway enrichment analysis (Fig. 3i). These
158 results suggest that the transcriptomic patterns of human ESCC are most similar to the
159 transcriptomic features of *Trp53*, *Cdkn2a*, *Notch1* tKO EOs.

160 ***Trp53* / *Cdkn2a* / *Notch1* tKO cells are tumorigenic *in vivo* via Ccl2-mediated immune**
161 **evasion**

162 Having determined that either PN dKO or PCN tKO is sufficient to induce the neoplastic
163 phenotype *in vitro* (Fig. 1, 2), we determined the impact of PN dKO and PCN tKO on ESCC
164 tumorigenesis *in vivo* by congenic transplantation. Intriguingly, only PCN cells developed tumors,
165 with a 60% success rate (3 of 5), while PN did not grow (0 of 5) in the immunocompetent
166 (C57BL/6) mice (Fig. 4a, b), which was unexpected considering the superior cell growth of PN
167 compared to that of PCN *in vitro* (Fig. 1k, l). PCN cell-derived tumors had substantially invaded
168 the muscular layer with poorly differentiated squamous cell carcinoma (Fig. 4b). PCN tumors were
169 hyperproliferative (Mki67), with ESCC stemness marker (Sox2 and Trp63) expression,
170 recapitulating the features of ESCC (Fig. 4c).

171 These results led us to hypothesize that PCN cells evade immune surveillance, while PN
172 cells are easily targeted by immune cells. Indeed, $Cd4^+$ T cells, $Cd8^+$ T cells, neutrophils, and
173 dendritic cells infiltrated into the PCN-derived tumors, implying an active interaction between
174 tumor and immune cells (Extended Data 4a). To test this, we comparatively examined PN and
175 PCN transcriptomes. An Enrichr analysis showed that the genes associated with T-cell receptor
176 signaling and antigen processing and presentation were highly enriched in the PCN compared to
177 the PN (Extended Data 4b). A DEG analysis of bulk RNA-seq showed that the genes related to
178 immune response and cytokine-related signaling pathways were highly expressed in PCN
179 compared to in PN (Fig. 4d and Extended Data 4c), suggesting that cytokines or chemokines
180 specifically expressed in PCN cells contribute to immune evasion. A comparative DEG analysis
181 of scRNA-seq data sets identified three cytokines (Ccl2, Cxcl1, and Cxcl2) that were highly
182 upregulated in PCN (Fig. 4e). Notably, only Ccl2 expression was specifically enriched in the PCN
183 compared to WT, PC, and PN (Fig. 4f and Extended Data 4d-h). Consistently, immunostaining
184 validated the high expression of Ccl2 in PCN allograft tumors and Ccr2, a receptor for Ccl2, in the
185 immune cells surrounding the tumor (Extended Data 4i).

186 Since CCL2 expressed by tumor cells is known to recruit myeloid cells (monocytes, tumor-
187 associated macrophages [TAMs], and myeloid-derived suppressor cells [MDSCs]) to the TME,
188 inhibiting the Ccl2-Ccr2 axis was shown to enhance the immune response to tumors[23-26]. To

189 determine the role of Ccl2 in immune evasion of PCN cells, we genetically ablated the *Ccl2* gene
190 in PCN cells (PCN-*Ccl2* KO) and compared tumorigenicity of PCN and PCN-*Ccl2* KO cells using
191 allograft transplantation. PCN and PCN-*Ccl2* KO showed no difference in cell growth *in vitro*
192 (Extended Data 5a, b). However, unlike PCN cells, PCN-*Ccl2* KO cells barely developed tumors
193 in immunocompetent mice (Fig. 4g-i). Although immune cells were abundant in both PCN parental
194 and *Ccl2* KO tumors, the keratin pearls, one of the signatures of ESCC, were mainly observed in
195 PCN tumors compared to *Ccl2* KO tumors, indicating that PCN tumors develop with less
196 interruption by immune cells (Extended Data 5c). In line with this, the number of exhausted T (T_{ex})
197 cells (expressing Pdcd1/Pd-1) was increased among the immune cells surrounding PCN tumors
198 compared to PCN-*Ccl2* KO tumors (Fig. 4j, k and Extended Data 5d). Moreover, PCN-*Ccl2* KO
199 tumors showed a higher number of cells with perforin, an effector $Cd8^+$ T cell marker, $Cd8^+$ T
200 cells, and cleaved-Caspase-3^+ (an apoptotic cell marker) cells compared to PCN tumors,
201 suggesting that more cell death mediated by T cells occurs in PCN-*Ccl2* KO tumors than in PCN
202 tumors (Fig. 4j, k and Extended Data 5d). Simultaneously, a more significant number of $Cd206^+$
203 (an M2 macrophage marker) cells was observed in PCN tumors than in PCN-*Ccl2* KO tumors (Fig.
204 4j, k and Extended Data 5d).

205 Although we found fewer M2 macrophage marker–expressing cells in PCN-*Ccl2* KO
206 tumors than in PCN tumors, we did not find significant differences in the number of M1
207 macrophage ($CD68^+$/$Cd80^+$ cells) or MDSC ($Cd11b^+$/$Ly6g^+$ cells) infiltration (Extended Data 5d-
208 f). Nonetheless, the proliferation of PCN and PCN-*Ccl2* KO tumors was comparable based on the
209 $Mki67^+$ cell quantification (Fig. 4j, k and Extended Data 5d). These results suggest that Ccl2
210 secreted from PCN tKO tumor cells contributes to immune evasion in ESCC tumorigenesis.

211 Emerging Ccl2-Ccr2 interaction between tumor and immune cells during ESCC 212 tumorigenesis

213 To complement allograft models, we analyzed single-cell transcriptomics of an autochthonous
214 mouse model[27]. In this model, treatment of 4-NQO (4-nitroquinoline 1-oxide) resulted in
215 development of inflammation, hyperplasia, dysplasia, cancer in situ, and invasive cancer in the
216 esophageal epithelium in a time-dependent manner. From the scRNA-seq datasets of the 4-NQO
217 model, the epithelial cells (proliferating, basal, suprabasal, stratified, and other cells) and the
218 immune cells (T, B, and myeloid cells) were sub-clustered based on marker gene expression
219 (Extended Data 6a-f). This ESCC model showed decreased expression of Trp53, Cdkn2a, and
220 Notch signaling pathways-related genes through ESCC development, similar to PCN organoids
221 (Extended Data 7a). A comparative analysis of epithelial cell transcriptomes at each stage with
222 ESCC patients showed increasing similarity as murine ESCC develops under 4-NQO exposure
223 (Extended Data 7b, c), suggesting that the 4-NQO mouse model recapitulates human ESCC
224 tumorigenesis. Notably, in hyperplasia, *Ccl2* and *Ccr2* expression was the highest in the
225 esophageal epithelial cells and immune cells, respectively (Fig. 5a, b and Extended Data 7d, e). A
226 further subtype analysis showed that *Ccr2* expression was enriched in the T_{ex} cells and regulatory
227 T (T_{reg}) cells (Extended Data 7f). Moreover, we found that T_{ex} cell marker (Cd160, Havcr2/Tim-
228 3, Pdcd1/Pd-1, and Lag3) expression was increased in the T cells at the early stage of ESCC
229 tumorigenesis (Extended Data 7g), consistent with our PCN-transplanted tumor cells (Fig. 4 and
230 Extended Data 5). To investigate the intercellular CCL-mediated ligand-receptor interaction,
231 epithelial and immune cell communications were analyzed using the Squidpy and CellChat

packages. The CCL2-CCR2 interaction was inferred to be strong from the hyperplasia state and maintained until invasive cancer (Fig. 5c). Moreover, the total interactions related to the CCL pathway between epithelial cells and immune cells were increased during ESCC development (Fig. 5d and Extended Data 7h). The CCL pathway–specified cell-cell communications were observed starting from the inflammation status in epithelial cells, T_{ex} cells, MDSCs, and macrophages (Fig. 5e and Extended Data 7i).

Given the role of the CCL2-CCR2 axis in the immune evasion of tumor cells[28], we tested whether the CCL2-CCR2 axis is indispensable for ESCC initiation using two different Ccr2 inhibitors (Ccr2 22 and BMS-813160). To increase tumorigenic efficiency, we established PCN cells that stably expressed Sox2 (PCNS) as Sox2 promotes ESCC tumorigenicity[29]. Sox2 overexpression accelerated the tumor development of PCN cells while not affecting Ccl2 expression (Extended Data 8a-c). Although Ccr2 inhibitors did not suppress PCNS cell growth *in vitro*, allograft tumors grown with Ccr2 inhibitors were drastically reduced in size and incidence compared to the tumors treated with vehicle (Fig. 5f and Extended Data 8d). All tumors that were exposed to vehicle and Ccr2 inhibitors showed abundant immune cell infiltration into the tumors and a comparable number of proliferating ($Mki67^+$) tumor cells (Extended Data 8e, f). Consistent with the *Ccl2* KO tumor results, T_{ex} cell ($Pdcd1^+$) infiltration into Ccr2-inhibited tumors was markedly decreased, while active $Cd8^+$ T cells ($perforin^+$ cells) were enriched in the tumors from Ccr2 inhibitor-injected mice compared to in the tumors from vehicle-injected control mice (Fig. 5g, h and Extended Data 8f, g). On the other hand, fewer M2 macrophages were observed in the Ccr2-inhibited tumors than in the *Ccl2* KO tumors (Fig. 5g, h and Extended Data 8f). However, the number of other monocyte-derived cells ($Cd68^+$ or $Cd209^+$) was lower in the Ccr2 inhibitor–treated TME, indicating reduced monocyte recruitment by Ccr2 blockade (Extended Data 8f, g). These results suggest that the CCL2-CCR2 axis elicits immune evasion for ESCC initiation.

NF-κB pathway, the upstream regulator of Ccl2

Next, we determined the mechanism of CCL2 upregulation during ESCC tumorigenesis. Given that CCL2 is upregulated mainly by transcription factors (TFs)[30], we sought to identify the key TFs that transactivate *CCL2*. An scRNA-seq-based regulon analysis identified PCN-specific regulons (RELA, FOXA1, MYC, TAF1, and TCF12) that may bind to the *CCL2* promoter (Extended Data 9a, b). Among them, Rela was the most highly activated in PCN, and the *Ccl2* gene is expected to be directly transactivated by Rela from a refined analysis using iRegulon (Extended Data 9c, d). Compared to PN, PCN cells showed more abundant nuclear accumulation of Rela and Rela inhibition downregulated *Ccl2* in PCN cells (Extended Data 9e, f). Moreover, a chromatin immunoprecipitation (ChIP) assay showed that Rela occupied the *Ccl2* promoter in PCN but not in PN cells, consistent with the results of a previous report that RELA transactivates *CCL2*[30,31] (Extended Data 9g). In addition, a human ESCC tissue microarray analysis showed a positive correlation between CCL2 and RELA expression, supporting the pathological relevance of the RELA-CCL2-CCR2 axis to human ESCC tumorigenesis (Extended Data 9h, i).

Classification of ESCC patients, and PCN relevance

271 To extend our findings to the biology of human ESCC tumorigenesis, we analyzed single-cell
272 transcriptomics of 69 ESCC patients (Fig. 6a). We integrated 69 human ESCC scRNA-seq datasets
273 with the murine PCN scRNA-seq dataset. The unsupervised principal components analysis and
274 Pearson correlation coefficient categorized 69 patient datasets into three groups (ESC1, 2, and 3).
275 While ESC1, 2, and 3 constituted a comparable portion of patients (ESC1: 30.4%; ESC2: 33.3%;
276 ESC3: 36.2%) with tumor cell heterogeneity as described previously[10], PCN belonged to ESC1
277 (Fig. 6b, c). Notably, the ESC1 displayed the lowest pathway score for TP53, CDKN2A, and
278 NOTCH signaling, suggesting that ESC1 has consistent transcriptomic features of PCN EOs (Fig.
279 6b, d). Furthermore, ESC1 and ESC2 showed the highest score for the NF-κB pathway, which was
280 correlated with *CCL2* expression (Fig. 6e, f). Consistent with our findings of the immune landscape
281 of PCN tumors, tumor cells of ESC1 patients expressed a higher level of CD274/PD-L1,
282 suggesting that PCN-type (ESC1) likely has immune escape potential through PD-L1-PD1-
283 mediated T cell exhaustion (Fig. 6f and Extended Data 10a). Of note, despite the transcriptomic
284 differences among the three groups of patients, we could not find categorical differences between
285 the conventional tumor stage classification and ESC1-3 groups (Extended Data 10b).

286 We further identified the representative marker genes of each group of patients by DEG
287 analysis. ESC1 showed higher expression of *B2M*, *RGS1*, and *THEMIS2*, which were reported to
288 be highly expressed in several types of cancer[32-34]. On the other hand, *PERP*, *KRT15*, and *CD9*
289 were highly expressed in ESC2, and *CD151*, *IGFBP4*, and *EID1* were enriched in ESC3 patients
290 (Fig. 6g, Extended Data 10d). Although these markers are upregulated in various cancers[35-40], they
291 have not been investigated in ESCC. ESCC patients with higher expression of *B2M*, *RGS1*,
292 *THEMIS2*, *PERP*, and *CD151* experienced poor survival compared to those with lower expression
293 (Extended Data 10d). A TCGA-based analysis also showed that B2M, RGS, PERP, KRT15, and
294 CD9 were upregulated in ESCC compared to normal samples (Extended Data 10e).
295 Immunostaining of the ESCC tissue microarray (n = 101) revealed a positive correlation between
296 B2M and CCL2 expression and B2M and RELA expression (Fig 6h, i, and Extended Data 10f).
297 Most patients (90.9%) showed relatively higher expression of B2M in tumor samples than in
298 adjacent normal samples, and 22.7% (5 of 22, immunohistochemistry score ≥ 2.5) of patients
299 showed robust expression of both CCL2 and B2M in the tumor tissue (Fig. 6k). Focusing on tumor
300 samples alone, 49.0% (25 of 51) of tumor samples expressed high levels of B2M
301 (immunohistochemistry score ≥ 2.5), a slightly higher proportion compared to the ESC1 from
302 scRNA-seq. These data suggest that B2M is a prognostic marker of ESCC likely with the RELA-
303 CCL2 axis activation.

Discussion

Understanding ESCC initiation may improve its early detection, diagnosis, and treatment. However, the biology of ESCC initiation remains elusive. Moreover, model systems that recapitulate ESCC initiation are not available. In this study, we found that the genetic inactivation of *TP53*, *CDKN2A*, and *NOTCH1* (PCN) induces esophageal neoplasia (cell-autonomous) and generates an immunosuppressive niche (non-cell-autonomous) to promote ESCC tumorigenesis.

To identify the multiple genetic factors responsible for ESCC initiation, we genetically engineered EOs with 32 different combinations of nine candidate tumor suppressor genes based on the genomics of ESCC patients. *Trp53*, *Cdkn2a*, and *Notch1* were found to be essential tumor suppressor genes associated with ESCC initiation. While PN and PCN EOs displayed the neoplastic features of ESCC *in vitro*, only PCN cells exhibited *in vivo* tumorigenicity, indicating the existence of PCN-driven immune evasion. Transcriptomic analysis identified that the CCL2-CCR2 axis remodels immune landscape in ESCC tumorigenesis, as confirmed by the loss-of-function studies (*Ccl2* KO and Ccr2 inhibitors) and a scRNA-seq analysis of the autochthonous mouse model. Finally, we used single-cell transcriptomics to stratify and identify a group of PCN-type ESCC patients with new biomarkers.

We selected organoids as a model system for multiple genetic manipulations, which overcomes the limitation of single-gene KO (e.g., CRISPR-based screening) and provides a better phenotype analysis (i.e., neoplasia). However, the pitfalls of the organoid model include the lack of a niche, including mesenchymal and immune cells, later complemented by our congenic transplantation approach (PN vs. PCN) (Fig. 4a-c). Although we determined that PCN was a minimal genetic combination for ESCC initiation, our approach did not test the impact of oncogenes (e.g., *SOX2*, *NFE2L2*, and *PIK3CA*) that were frequently hyperactivated in ESCC. Indeed, the introduction of *SOX2*, which was amplified in 40% of ESCC patients[29], or $Kras^{G12D}$ accelerated *in vivo* tumorigenesis[19] (Extended Data 8b). Therefore, the combinatorial effects of tumor suppressor genes and oncogenes in ESCC tumorigenesis remain to be determined.

Single-cell transcriptomics has deepened our understanding of ESCC tumorigenesis. An scRNA-seq analysis unraveled distinct cell lineage trajectories and higher cell plasticity generated by PCN (Fig. 2e-i). Whereas WT organoids bear a single root cell cluster that differentiates into other cell clusters, PCN organoids harbor multiple root cell clusters that generate complicated and interconnected cell lineage trajectories, somewhat recapitulating the multiple clonal expansion and tumor heterogeneity of human cancer (Fig. 2h, i). Furthermore, single-cell transcriptomics expanded our experimental findings to stratifying ESCC patients. Unlike bulk RNA-seq, scRNA-seq allowed us to analyze tumor cells, excluding infiltrated immune cells. Despite the inter-tumoral heterogeneity of patient tissue samples, ESCC patients were classified into three groups based on the single-cell transcriptional signatures of tumor cells. ESC1 ESCC patients were highly correlated with murine PCN. These well-matched results are striking because a single-cell transcriptomics-based comparison of models (mice and organoids) in ESCC patients not only identifies key genetic factors (PCN) for ESCC tumorigenesis but also validates model systems, which could be further improved by precise mouse-to-human gene conversion and more patient datasets. Nonetheless, inter-tumoral heterogeneity remains to be addressed based on our ESCC classification.

346 Tumor cells evade immune surveillance in various ways[41,42]. Despite several studies
347 describing the immune landscape of ESCC based on single-cell transcriptomics[9,10,43], experimental
348 demonstration of ESCC immune evasion was not achieved. In this study, our comprehensive
349 approaches discovered that *CDKN2A* inactivation plays a key role in establishing tumor-favorable
350 immune cell niche. scRNA-seq-based immune profiling of the mouse ESCC model showed
351 decreased effector T cells and increased immune suppressive dendritic cells during ESCC
352 development[44], consistent with our finding (Fig. 4j, k and Extended Data 6e, f). Similarly, human
353 ESCC generates an immune-suppressive landscape with enriched T_{ex} or T_{reg} cells and upregulation
354 of immunosuppression-related genes in TAMs and dendritic cells[10,11,43]. Notably, enriched T_{ex}
355 cells and TAMs are commonly observed in mouse scRNA-seq-based immune profiling and PCN
356 TME (Fig. 4j, k and Extended Data 6e, f), unveiling the immune niche of at least PCN-associated
357 ESCC tumorigenesis.

358 We found that CCL2 is the key immune landscape remodeling factor for ESCC initiation,
359 as represented by increased T_{ex} cells and M2-like macrophages and a reduced number of effector
360 $Cd8^+$ T cells and dendritic cells. The CCL2-CCR2 axis modulates the TME to be favorable to
361 tumor cells[45]. Given the high expression of CCR2 in monocytes, CCR2-mediated M2-like
362 macrophage differentiation and polarization had been extensively studied in the context of tumor
363 cell invasion and metastasis[25]. In addition, the CCL2-CCR2 axis was shown to induce ESCC
364 immune evasion via TAM accumulation[28]. Moreover, CCR2 expressed in T cells modulates the
365 recruitment of T_{reg} cells[46], hampering immune surveillance. Therefore, targeting CCL2 to enhance
366 the immune response to tumor development may be a promising option for ESCC treatment.
367 Indeed, targeting the CCL2-CCR2 axis has been actively tested in clinical trials in other types of
368 cancer, with or without immune checkpoint inhibitors (ICIs)[26,45,47]. However, it should be noted
369 that since CCL2 is a chemoattractant that recruits monocytes, systemic inhibition of CCL2-CCR2
370 might affect normal immune surveillance. For instance, impaired monocyte recruitment by *Ccr2*
371 blockade could reduce the number of antigen-presenting cells, diminishing innate and adaptive
372 immune responses that are critical for anti-cancer effects[48]. Our results showed that the transient
373 inhibition of Ccr2 suppressed tumor growth, but monocyte-derived cell ($Cd209^+$ or $Cd68^+$)
374 recruitment was decreased while the number of $Cd8^+$ T cells was not significantly increased
375 compared to the TME of *Ccl2* KO tumors (Fig. 5 and Extended Data 8). Therefore, targeting CCL2
376 or the upstream molecules of CCL2 in tumor cells would minimize potential adverse effects.

377 Recent clinical trials showed promising outcomes of ICIs in patients with advanced
378 ESCC[12-16]. Nonetheless, ESCC patient stratification is a significant hurdle. Although the datasets
379 from the 69 patients analyzed in this study lacked ICI-related clinical information, PCN-type
380 (ESC1) patients showed higher expression of PD-L1/CD274 than did other patients. Thus, in
381 addition to blocking the CCL2-CCR2 axis, ICIs targeting PD-L1 or PD-1 can be effective in ESC1
382 patients, and B2M could be a biomarker for ESC1-type patients (Fig. 6g and Extended Data 10c).
383 Therefore, our study also proposes a new biomarker-guided strategy for treating PCN-type ESCC
384 patients with ICIs (PD-L1 or PD-1 inhibitors) or CCL2 blockers.

385 Together, this study identifies the inactivation of *TP53*, *CDKN2A*, and *NOTCH1* as the key
386 genetic event leading to ESCC development accompanied by immune evasion and newly classifies
387 ESCC patients for better outcomes of immunotherapy.

388

Author contributions

K.-P.K. and J.-I.P. conceived the experiments. K.-P.K. and J.-I.P. designed the experiments. K.-P.K., Y.H., B.K., S.Z., G.Z., J.Z., and S.J. performed the experiments. K.-P.K., H.N., and J.-I.P. analyzed the data. C.M., K.J.D., G.E., A.-K.R., and H.N. provided ESCC samples. K.-P.K. and J.-I.P. wrote the manuscript.

Acknowledgments

We are grateful to Kwon-Sik Park, Pierre D. McCrea, and Malgorzata Kloc for insightful comments, Ann Sutton (Research Medical Library, MD Anderson) for editing the manuscript, and the Herbert Irving Comprehensive Cancer Center for the shared resources (Biostatistics, Genomics, and Molecular Pathology, and 3D organoid/cell culture). This work was supported by the Cancer Prevention and Research Institute of Texas (RP200315 to J.-I.P.), the National Cancer Institute (CA193297 and CA256207 to J.-I.P; 5P30CA013696 and 5P01CA098101 to A.-K.R., H.N., K.D., G.E., C.M.), an Institutional Research Grant (MD Anderson to J.-I.P.), a Specialized Program of Research Excellence (SPORE) grant in endometrial cancer (P50 CA83639), and Radiation Oncology Research Initiatives. The core facilities at Baylor College of Medicine (Cytometry & Cell Sorting Core and Single Cell Genomics Core) were supported by CPRIT (RP180672, RP200504) and the National Institutes of Health (CA125123, RR024574).

408 **Methods**
409
410 **Mice**
411 C57BL/6, *Trp53*$^{floxed/floxed}$ (JAX no. 008462), and *Rosa26*$^{nT\text{-}nG}$ (JAX No. 023035) mice were
412 purchased from the Jackson Laboratory. Mice were bred and housed in an air-conditioned room
413 of the Division of Laboratory Animal Resources facility at The University of Texas MD Anderson
414 Cancer Center on a 12-hr light/dark cycle. All animal procedures were performed in accordance
415 with the guidelines of the Association for the Assessment and Accreditation of Laboratory Animal
416 Care and institutionally approved protocols (MD Anderson Institutional Animal Care and Use
417 Committee). The study was compliant with all relevant ethical regulations regarding animal
418 research.
419
420 **Wnt3A, R-Spondin1, and Noggin conditioned medium**
421 The Wnt3A, R-Spondin1, and Noggin (WRN) conditioned medium was prepared as previously
422 described[49]. In brief, L-WRN (ATCC CRL-3276) cells were cultured on a 10-cm plate with culture
423 medium (Dulbecco's modified Eagle's medium [DMEM], 0.5 mg/mL G418, 0.5 mg/mL
424 hygromycin B, 1% penicillin/streptomycin, and 10% fetal bovine serum [FBS]). After 10% of L-
425 WRL cells had been seeded in culture medium (without G418 and hygromycin B) in 10-cm plates,
426 cells were incubated for 3-4 days. The medium was replaced with 10 mL of fresh medium when
427 the cells were 80%-90% confluent, and the cells were incubated for 24 hrs. The medium was
428 collected, centrifuged at 1000 × g for 4 min, passed through a 0.22-μm sterile filter, and stored at
429 −80 °C. Another 10 mL of fresh medium was added to the plates and collected after 24 hrs to make
430 the second batch of conditioned medium using the same procedures. The first, second, and third
431 batches of conditioned media were mixed before use to prepare a 100% WRN conditioned medium.
432
433 **Esophageal tissue isolation**
434 The cervical dislocation was performed after the 8- to 10-week-old mice had been euthanized via
435 CO2 inhalation. The esophagi were collected in 10-cm Petri dishes with ice-cold phosphate-
436 buffered saline (PBS) with 1% penicillin/streptomycin and swirled gently to remove blood. The
437 esophagi were opened longitudinally and washed with cold PBS with 1% penicillin/streptomycin.
438 The epithelial cell layer was peeled off using surgical tweezers and then dissected into 0.5-cm3
439 pieces with surgical blades. The minced esophagi were collected in a 15-mL conical tube and
440 digested by 0.05% trypsin-EDTA at 37 ℃ for 60 min with frequent vortexing. After dissociation,
441 3× volume 10% FBS-supplemented DMEM was added to inactivate the dissociation enzyme,
442 followed by vigorous pipetting. The suspension was passed through a 35-μm sterile cell strainer
443 to collect a single-cell suspension. Finally, the cell suspension was spun down at 1000 rpm for 4
444 min at ambient temperature and resuspended in a 50% WRN-conditioned medium.
445
446 **EO culture**
447 The E-MEOM included 50% WRN medium (50% advanced DMEM/F12, 50% WRN conditioned
448 medium, 1% penicillin/streptomycin, and 1 × GlutaMAX), 1 × B27, 50 ng/mL, 10 mM
449 nicotinamide, 500 nM A83-01, 10 μM SB202190, 50 ng/mL EGF, and 10 μM Y-27632 ROCK
450 inhibitor (first 3 days). Single-cell dissociated esophageal epithelial cells (1000 cells) were
451 suspended in 8 μL of E-MEOM and 12 μL of pre-thawed Matrigel (Corning) on ice and seeded in
452 the centers of a well to create a Matrigel dome. The plate was incubated at 37 °C for 10 min to
453 solidify the Matrigel. Finally, 500 μL of E-MEOM was added and incubated at 37 °C with 5%

454 CO2. The medium was changed every 2-3 days. See Supplementary Table 1 for reagents
455 information.
456
457 ***Trp53KO* EO**
458 8- to 10-week-old *Trp53*$^{floxed/floxed}$ mice were euthanized to collect the esophagi, which were
459 digested into a single-cell suspension and seeded in Matrigel to form EOs, as described above.
460 After 7 days of culture, EOs were digested with 0.05% trypsin-EDTA at 37 °C for 45 min to create
461 a single-cell suspension. Ad-CMV-EGFP or Ad-Cre-EGFP (University of Iowa) was added to the
462 cell suspension at 1 × 103 pfu/cell. Cells were then suspended in Matrigel to generate new EOs.
463 After 2 days of seeding, 10 μM nutlin3 was added for *Trp53*$^{floxed/floxed}$ cell selection. Two days later,
464 the selection was performed by sorting the GFP+ cells after dissociating EOs into single cells, and
465 the sorted cells were re-seeded for EO culture as described above. EOs were collected for
466 genotyping 7 days after seeding. Wild-type, *Trp53*$^{floxed/floxed}$, and KO Trp53 alleles were amplified
467 as 288 bp, 370 bp, and 612 bp, respectively. See Supplementary Table 2 for primer information.
468
469 **CRISPR/Cas9-based gene KO in EOs**
470 CRISPR/Cas9 system-mediated gene KO was described in a previous study[50]. In brief, WT or
471 Trp53 KO EOs were digested with 0.05% Trypsin-EDTA to dissociate into single cells. Single
472 cells were incubated with a virus-containing medium with polybrene for 1 hr with centrifugation
473 (600 g) at 32 °C (see Supplementary Table 3 for sgRNA sequences). Cells were then incubated at
474 37 °C with 5% CO2 for 4 more hrs and embedded in Matrigel. The medium was replaced 2 days
475 after infection with antibiotics (puromycin, blasticidin, or hygromycin) for selection. Gene KO
476 was confirmed by genomic DNA PCR after lysis of the organoid using specific primer pairs (see
477 Supplementary Table 2 for primer information).
478
479 **Sox2 stable cell line establishment**
480 Sox2 overexpressing PCN cells were established by Lenti-viral transduction. Briefly, pLenti-
481 Sox2-GFP plasmid was prepared by amplifying Sox2 template from the pLV-tetO-Sox2
482 plasmid(addgene, #19765), and then transferred to pLenti CMV GFP plasmid (addgene, #17446)
483 using High-Fidelity DNA polymerase (NEB). Viral transduction was performed as described in a
484 previous study[50]. GFP fluorescence expressing cells were isolated using flow cytometry (BD
485 FACSAria II Cell Sorter) and cultured again.
486
487 **Organoid-forming efficiency and size analysis**
488 After 7 days of organoid seeding in Matrigel, the size of the organoids was analyzed by measuring
489 the volume under the microscope (ZEN software, ZEISS). To reduce the vulnerability of EOs, the
490 measurements were performed after at least 3 passages after isolation from the KO experiments.
491 All experiments included more than 50 organoids per group.
492
493 **H&E, PAS, and immunofluorescence staining**
494 All staining was performed as previously described[51]. 7 days after seeding, EOs were collected by
495 dissociating Matrigel using ice-cold PBS and fixed in 4% paraformaldehyde at ambient
496 temperature. For tumor tissue, excised tumors were washed with ice-cold PBS and fixed with
497 formaldehyde at ambient temperature. After paraffin embedding, tumor tissue and organoid
498 sections were mounted on glass slides. For H&E staining, sections were incubated in hematoxylin
499 for 3-5 min and eosin Y for 20-40 s. For PAS staining, slides were immersed in the periodic acid

solution for 5 min at ambient temperature and then in Schiff's reagent for 15 min at ambient temperature, followed by hematoxylin solution for 60-90 s. After washing with tap water, slides were dried, and the coverslips were mounted with mounting media. For immunofluorescence, after blocking with 3% goat serum in PBS for 30 min at ambient temperature, sections were incubated with primary antibodies (Krt13 [1:250], MKi67 [1:250], Sox2 [1:250], Trp63 [1:250], cleaved caspase-3 [1:250], Rela [1:200], Pdcd-1/Pd-1 [1:200], perforin [1:200], Cd8 [1:200], Cd206 [1:200], Cd209 [1:200], Havcr2/Tim3 [1:200], Cd4 [1:200], Mpo [1:200], Ccl2 [1:200], Ccr2 [1:200], Cd3 [1:200], Cd68 [1:200], Cd11b [1:100], Ly6g [1:100], and Cd80 [1:200]) overnight at 4 °C and secondary antibody (1:250) for 1 hr at ambient temperature. Sections were mounted with ProLong Gold antifade reagent with DAPI (Invitrogen). Images were captured with the fluorescence microscope (Zeiss; AxioVision). See Supplementary Table 1 for antibody information.

Immunohistochemistry

ESCC cancer tissue microarray slides contained 144 samples from 55 patients (provided by Dr. Hiroshi Nakagawa). Immunostaining was performed as previously described[51]. In brief, paraffin-embedded tissue antigens were retrieved with a basic or citrate antigen retrieval buffer. After being blocked with goat serum in PBS, tissues were incubated with primary antibodies (CCL2/MCP-1 [1:200], RELA [1:200], and B2M [1:200]). The immunohistochemistry results were scored, analyzed, and visualized using the "gglot2" package in r and GraphPad Prism (v9.2.0).

Gene expression analysis

Organoids were harvested and lysed, and RNAs were extracted by TRIzol reagent. RNA was quantified with a Nanodrop 2000c Spectrophotometer (Thermo Scientific) and then converted to cDNA using SuperScript II reverse transcriptase with random hexamers. PCR amplification (StepOne Real-Time PCR System, Applied Biosystems) was performed using the following conditions: 95 °C for 10 min, 95 °C for 15 s (denature), and 60 °C for 1 min (anneal/extend) for 40 cycles; 95 °C for 15 s and 60 °C for 1 min; and 95 °C for 15 s (melting curve). qRT–PCR results were quantified by comparative $2^{-\Delta\Delta Ct}$ methods (see Supplementary Table 2 for primer information). The results were expressed as average fold change in gene expression and were normalized to the expression of mHprt.

BrdU incorporation assay

Organoids were incubated with BrdU (10 μM) for 0.5 hr from 7-day cultured organoids. BrdU-containing medium was removed, and Matrigel-embedded organoids were harvested. EOs were washed three times with PBS and fixed with 4% PFA for 30 min at ambient temperature. After the paraffin-embedding process, slides were prepared for staining. Following the immunofluorescence staining method, the slides were incubated with BrdU antibody at 4 °C and fluorescence-conjugated secondary antibody. Samples were further stained with DAPI and mounted for imaging.

Organotypic co-culture

Four-well chamber slides (Falcon) were coated with 200 μg/mL Matrigel and stored at 4 °C until cell seeding. Stromal cells from esophagi were isolated from Rosa26nT-nG mice. We collected the stromal cell layer by peeling off the epithelial cells from the longitudinally cut esophagi. Stromal cells were dissociated with collagenase/dispase for 1 hr at 37 °C and passed through a 70-μm cell strainer. After counting, cells (1.2 × 105 cells/well) were seeded in the pre-warmed

546 Matrigel-coated chamber. Cells were grown with DMEM supplemented with 20% FBS for 14 days.
547 Epithelial cells were collected from WT, PN, and PCN organoids and seeded on the stromal cell–
548 cultured chamber slide. The medium was replaced every 2 days and cultured for 14 days. For
549 staining, cells were fixed with 4% PFA for 30 min at ambient temperature and then incubated with
550 Cdh1 (1:200) overnight at 4 °C. Cells were visualized using secondary antibodies conjugated with
551 fluorescein (1:200) for 1 hr at ambient temperature, and the images were taken with a fluorescence
552 microscope (ZEISS; AxioVision).
553
554 **2D culture**
555 EOs were digested with 0.05% trypsin-EDTA at 37 °C for 45 min to create a single-cell suspension
556 in a 15-mL centrifuge tube. The cells were centrifuged down at 1000 rpm for 4 min at ambient
557 temperature, suspended in DMEM + 10% FBS with 10 μM Y-27632, and seeded on a 24-well
558 plate. Cells were passaged every 3-5 days. After the third passage, Y-27632 was removed from
559 the culture medium. DMEM supplemented with 10% FBS and 10% DMSO was used to freeze
560 cells and store them in liquid nitrogen.
561
562 **Colony formation, cell growth, wound-healing assays**
563 Cells (1 × 104) were seeded on a 60-mm dish, and the medium was replaced every 2 days. The
564 cells' colony-forming ability was monitored, and they were fixed with methanol for 20 min. The
565 fixative was removed, and the dishes were rinsed with distilled water. The colonies were stained
566 with 0.05% crystal violet solution, and the dishes were dried after being washed three times with
567 distilled water. For the cell growth analysis, 2 × 105 cells were seeded on the 60-mm dish. The
568 cell number was measured every day using an automated cell counter (Biorad) after the cells were
569 trypsinized and stained with Trypan Blue. For the wound-healing assay, 1 × 104 cells were seeded
570 on the 24-well plate. A wound was made in the middle of the well after the cells were confluent,
571 and the cells were imaged at 0, 8, and 20 hr.
572
573 **Xenograft and allograft transplantation**
574 Five-week-old BALB/c nude mice and C57BL/6 mice were maintained in the Division of
575 Laboratory Animal Resources facility at MD Anderson. 2D-cultured PN, PCN, PCN-Ccl2 KO,
576 PCNS, and PCNS-Ccl2 KO cells (3 × 106) were injected subcutaneously into the right dorsal
577 flanks of mice, respectively. Tumor volume was calculated by measuring with calipers every 3-4
578 days (volume = (length × width2)/2). For Ccr2 inhibitor treatment, DMSO-dissolved BMS Ccr2
579 22 (1 mg/kg) and BMS-813160 (25 mg/kg) were injected intraperitoneally at day 17, 21, and 25.
580 DMSO was injected as vehicle control. Mice were euthanized, and tumors were collected at day
581 57. The excised tumors were photographed and paraffin-embedded for immunostaining.
582
583 **Library preparation for RNA-seq and scRNA-seq**
584 For bulk RNA-seq, triplicated WT, PN, and PCN organoids were harvested 7 days after seeding
585 and lysed using the RNeasy Plus Mini Kit (QIAGEN). Purified RNA was used for mRNA library
586 preparation, sequenced by Illumina NovaSeq, and mapped to GRCm38/mm10 genome
587 (Novogene).
588 For scRNA-seq, organoids from WT, PC, PN, and PCN were collected 7 days after seeding
589 and digested with 0.05% trypsin-EDTA at 37 °C for 30 min. After trypsin had been inactivated
590 with 10% FBS DMEM, a single-cell suspension was collected by passing cells through a 35-μm
591 cell strainer. Each group was tagged with two CMO tags from the CellPlex kit (10× Genomics).

592 The tagged cells of each group were pooled together with the same number of cells after being
593 counted. The cDNA library was prepared with the 10× Genomics 3' v2 kit and sequenced on an
594 Illumina NovaSeq (Novogene), mapped to the GRCm38/mm10 genome, and demultiplexed using
595 CellRanger. The resulting count matrices files were analyzed in R (Seurat) or Python (Scanpy).
596
597 **Public scRNA-seq data preparation**
598 **Mouse datasets.** Mouse 4-NQO-treated scRNA-seq datasets were obtained from the Genome
599 Sequence Archive in BIG Data Center (Beijing Institute of Genomics, Chinese Academy of
600 Sciences, http://gsa.big.ac.cn) under the accession number CRA002118. Mouse datasets were
601 directly used for analysis as downloaded, with filtered matrices.
602
603 **Human datasets.** ESCC patient datasets were downloaded from the National Center for
604 Biotechnology Information Sequence Read Archive under the accession numbers
605 PRJNA777911 and PRJNA672851. ESCC patient datasets were downloaded and converted to
606 fastq files using Sequence Read Archive tools and the parallel-fastq-dump package. The
607 converted fastq files were used as input for the CellRanger (v6.1.2) pipeline. Analyses were
608 conducted with CellRanger output files. The datasets from 11 patients (PRJNA777911) and
609 tumor samples that had been previously sorted by Cd45− selection from 58 patients
610 (PRJNA672851) were input to run CellRanger (v7.0.1). Patient ID and tumor grade are
611 described in Supplementary Table 5.
612
613 **scRNA-seq data analysis**
614 **integration and clustering.** Organoid scRNA-seq data analysis. For pre-processing and
615 clustering of scRNA-seq data, we used the Seurat R package and Python package Scanpy. For
616 the organoid datasets, since two tags were used for one group of organoids, two datasets of the
617 same genotype were integrated using "sctransform" in Seurat and "concatenate" in Scanpy and
618 then annotated as WT, PC, PN, or PCN. The batch correction was performed in Scanpy using
619 "Harmony". UMAP was used for dimensional reduction, and cells were clustered into 35
620 groups in Seurat. Each cluster was annotated based on marker gene information. Seurat was
621 used for 4-NQO-treated mice datasets that had been sorted with $Cd45^-$ and $Cd45^+$ cells. Datasets
622 were pre-processed, normalized separately, and annotated based on their marker gene
623 expression. Disease status was annotated by converting the original implemented identity class,
624 "X0W, X12W, X20W, X22W, X24W, X26W" to "Normal, Inflammation, Hyperplasia,
625 Dysplasia, CIS, and Invasive cancer". Scanpy was used for human datasets preprocessing and
626 integration. Each dataset was normalized separately and clustered by the "Louvain" algorithm.
627 The clusters expressing a high level of PTPRC were removed to exclude immune cell
628 contamination and then a total 69 patient datasets were integrated using the "concatenate"
629 function. Batch effects were corrected using "Harmony". See Supplementary Table 6 for cell
630 numbers in each cell cluster.
631
632 **Proportion difference test.** The differences between the clusters from the two datasets were
633 tested using the scProportionTest package. The cluster difference between the two datasets was
634 compared, and the significance was calculated from the *P* value and confidence interval for the
635 magnitude difference via bootstrapping using the default parameter of permutation (n = 1000).
636

637 **Trajectory inference.** RNA velocity was used for cell lineage tracing and latent time inference
638 based on the results of previous report[52]. Bam files produced from the CellRanger pipeline were
639 used to create Loom files. Using the Python-based velocyto package, we produced Loom files
640 that included unspliced and spliced read information. Two Loom files were generated for one
641 genotype of organoid since the multiplex process had used two oligo tags for each genotype.
642 The Loom files from the same genotype were merged using the "combine" function in the
643 Loompy package. Cells were filtered, and dimensional reduction was performed following the
644 default parameters using the scVelo and Scanpy packages. RNA velocity was calculated
645 through a dynamical model, and cells were clustered using the "Louvain" algorithm. RNA
646 velocity for all four datasets was performed with the same parameters (n_neighbors=10,
647 n_pcs=50). Latent time analysis and a PAGA analysis were performed and plotted using the
648 scVelo package.
649
650 **Enrichr analysis.** To perform Enrichr analysis of PCN- or PN-enriched genes, we performed
651 DEG analysis from bulk RNA-seq and scRNA-seq results. DESeq2 package was used for bulk
652 RNA-seq and PCN highly expressed 1516 genes were used as input gene list. For scRNA-seq
653 data, 'FindMarkers' function was used to make DEG list from proliferating cell clusters of PCN
654 and PN datasets. 100 genes highly expressed in PCN compared to PN were used for Enrichr
655 analysis. The analysis was conducted following instructions as described[53]. See Supplementary
656 Table 7 and 8 for DEG results.
657
658 **fGSEA analysis.** To perform a GSEA of PCN- or PN-enriched genes with human ESCC samples,
659 we prepared a rank gene list from the DEG analysis of human ESCC vs. normal RNA-seq data
660 (TCGA). The "glmLRT" method was used, and the fdr cut-off was 0.05. We collected 495
661 ESCC highly expressed genes and 258 normal highly expressed genes and filtered the not-
662 assigned genes, resulting in 750 genes for analysis. The geneset was created from PCN or PN
663 organoid highly expressed genes compared to WT organoid expressed genes from scRNA-seq
664 data. To match the names of genes in the rank gene list and geneset, we converted mouse gene
665 names to human gene names using the biomaRt package. In total, 2812 PCN and 1285 PN
666 highly expressed genes were used to create genesets. The enrichment value was calculated and
667 plotted with the fgsea package (permutation number = 2000).
668
669 **Similarity test.** The Scissor package was used to compare the transcriptome of the organoids
670 scRNA-seq dataset and the bulk RNA-seq datasets of ESCC patients[54]. To compare scRNA
671 datasets with ESCC patients, we downloaded ESCC patient data and normal sample HTSeq
672 count data from the GDC data portal (TCGA-ESCA). After preparing the normal and ESCC
673 gene expression matrix, we converted the human gene names to mice gene names using the
674 biomaRt package. Not converted or assigned genes and duplicated gene names were removed
675 from the matrix, and a Scissor analysis was performed with each scRNA dataset using the Cox
676 regression model (alpha = 0.01). To compare scRNA-seq data with poor survival patient data,
677 we downloaded ESCC patients' clinical metadata from the GDC data portal and binarized it
678 into "poor survival" and "better survival". A Scissor analysis was conducted with scRNA
679 datasets using the Cox regression model and 0.03 alpha value.
680
681 **Regulon analysis.** For the regulon analysis in organoids, we used the pySCENIC package[55]. The
682 Loom file of each organoid dataset was used, and the regulon-based UMAP was redrawn after

683 binarization of each cell with regulons and an AUCell calculation. The AUCell of each regulon
684 and cell cluster were combined to obtain a regulon specificity score, and we found the top
685 regulons of each cluster. These processes were repeated five times in each organoid dataset
686 (WT, PC, PN, and PCN). To find the Ccl2 relevance, we created modules of candidate
687 transcription factors (Rela, Foxa1, Myc, Taf1, and Tcf12) in the PCN dataset. Transcription
688 factors and their target genes were calculated and visualized using Cytoscape.
689
690 **Cell-to-cell interaction analysis.** CellChat and Squidpy packages were used for the cell-to-cell
691 interaction inference. Epithelial cells, fibroblasts, and immune cell datasets were merged at each
692 disease stage to generate gene expression matrices for the CellChat analysis. The merged Seurat
693 objects were converted to an H5ad file for the Squidpy analysis. In the CellChat, the "CCL"
694 pathway was specified for analysis. "Epithelial cell" was defined as a "source group" and "T
695 cell", "myeloid cell", and "B cell" were selected as "target groups" in the Squidpy analysis
696 (permutation = 100, *P* value threshold = 0.05).
697
698 **Pathway score analysis.** We used Scanpy with the "scanpy.tl.score_genes" function for the
699 pathway score analysis. The analysis was performed with default parameters and the reference
700 genes from the gene ontology biological process or the Kyoto Encyclopedia of Genes and
701 Genomes database. The gene list for the score analysis is shown in Supplementary Table 9.
702
703 **Chromatin immunoprecipitation assay**
704 A chromatin immunoprecipitation (ChIP) assay was performed as previously described[56]. In brief,
705 PCN cells were harvested after being crosslinked with 1% formaldehyde for 10 min at ambient
706 temperature, followed by quenching with glycine (final concentration = 0.125M). Cells were lysed
707 and subjected to sonication (15 rounds of 30 sec on and 30 sec off, Bioruptor 300 [Diagenode]).
708 Lysates were cleared and incubated with pre-conjugated RELA antibody-Dynabeads overnight at
709 4 °C. Immunoprecipitates were washed and eluted, followed by incubation with RNase. After
710 RELA protein degradation with Proteinase K, ChIP DNA was purified using a PCR purification
711 kit (QIAGEN, #28106). Putative RELA binding sites of CCL2 promoter regions (region 1: -673~-
712 683, region 2: -1803~-1813, and region 3: -2035~-2045) and non-specific regions (-9708~-9838)
713 as a negative control were subjected to ChIP-qPCR. The primers for ChIP-qPCR are listed in
714 Supplementary Table 2.
715
716 **Kaplan-Meier analysis**
717 The overall survival of ESCC patients based on gene expression was determined using a publicly
718 available database (Kaplan-Meier Plotter, http://kmplot.com/analysis). Eighty-one ESCC patients
719 were divided into "high" and "low" groups by the median expression of the gene of interest. The
720 overall survival of the patient groups was compared for 70 months, and the log-rank *P* value is
721 marked in the figure.
722
723 **Statistical analysis**
724 The Student's *t*-test was used for comparisons of two groups ($n \geq 3$), and one-way analysis of
725 statistical variance evaluation was used for comparisons of at least three groups ($n \geq 3$). *P* values
726 < 0.05 were considered significant. Error bars indicate the standard deviation (s.d.). All
727 experiments were performed three or more times independently under identical or similar
728 conditions.

Data availability

Bulk and scRNA-seq data are available via the Gene Expression Omnibus (GSE 213929; http://https://www.ncbi.nlm.nih.gov/geo/query/acc.cgi?acc=GSE213929).
(Log-in token for reviewers:)

Code availability

The code used to reproduce the analyses described in this manuscript can be accessed via GitHub (https://github.com/jaeilparklab/ESCC_project_1) and is available upon request.

References

1 Pennathur, A., Gibson, M. K., Jobe, B. A. & Luketich, J. D. Oesophageal carcinoma. *The Lancet* **381**, 400-412, doi:10.1016/s0140-6736(12)60643-6 (2013).

2 Wang, G. Q. *et al.* Histological precursors of oesophageal squamous cell carcinoma: results from a 13 year prospective follow up study in a high risk population. *Gut* **54**, 187-192, doi:10.1136/gut.2004.046631 (2005).

3 Bejarano, L., Jordao, M. J. C. & Joyce, J. A. Therapeutic Targeting of the Tumor Microenvironment. *Cancer Discov* **11**, 933-959, doi:10.1158/2159-8290.CD-20-1808 (2021).

4 Hinshaw, D. C. & Shevde, L. A. The Tumor Microenvironment Innately Modulates Cancer Progression. *Cancer Res* **79**, 4557-4566, doi:10.1158/0008-5472.CAN-18-3962 (2019).

5 Keskin, D. B. *et al.* Neoantigen vaccine generates intratumoral T cell responses in phase Ib glioblastoma trial. *Nature* **565**, 234-239, doi:10.1038/s41586-018-0792-9 (2019).

6 Friedl, P. & Alexander, S. Cancer invasion and the microenvironment: plasticity and reciprocity. *Cell* **147**, 992-1009, doi:10.1016/j.cell.2011.11.016 (2011).

7 Baba, Y. *et al.* Tumor immune microenvironment and immune checkpoint inhibitors in esophageal squamous cell carcinoma. *Cancer Sci* **111**, 3132-3141, doi:10.1111/cas.14541 (2020).

8 Luan, S. *et al.* Advances in Drug Resistance of Esophageal Cancer: From the Perspective of Tumor Microenvironment. *Front Cell Dev Biol* **9**, 664816, doi:10.3389/fcell.2021.664816 (2021).

9 Chen, Z. *et al.* Dissecting the single-cell transcriptome network underlying esophagus non-malignant tissues and esophageal squamous cell carcinoma. *EBioMedicine* **69**, 103459, doi:10.1016/j.ebiom.2021.103459 (2021).

10 Zhang, X. *et al.* Dissecting esophageal squamous-cell carcinoma ecosystem by single-cell transcriptomic analysis. *Nat Commun* **12**, 5291, doi:10.1038/s41467-021-25539-x (2021).

11 Zheng, Y. *et al.* Immune suppressive landscape in the human esophageal squamous cell carcinoma microenvironment. *Nat Commun* **11**, 6268, doi:10.1038/s41467-020-20019-0 (2020).

12 Wang, Z. X. *et al.* Toripalimab plus chemotherapy in treatment-naive, advanced esophageal squamous cell carcinoma (JUPITER-06): A multi-center phase 3 trial. *Cancer Cell* **40**, 277-288 e273, doi:10.1016/j.ccell.2022.02.007 (2022).

13 Sun, J. M. *et al.* Pembrolizumab plus chemotherapy versus chemotherapy alone for first-line treatment of advanced oesophageal cancer (KEYNOTE-590): a randomised, placebo-controlled, phase 3 study. *Lancet* **398**, 759-771, doi:10.1016/S0140-6736(21)01234-4 (2021).

14 Doki, Y. *et al.* Nivolumab Combination Therapy in Advanced Esophageal Squamous-Cell Carcinoma. *N Engl J Med* **386**, 449-462, doi:10.1056/NEJMoa2111380 (2022).

15 Yamamoto, S. & Kato, K. JUPITER-06 establishes immune checkpoint inhibitors as essential first-line drugs for the treatment of advanced esophageal squamous cell carcinoma. *Cancer Cell* **40**, 238-240, doi:10.1016/j.ccell.2022.02.009 (2022).

16 Okada, M. *et al.* Three-Year Follow-Up and Response-Survival Relationship of Nivolumab in Previously Treated Patients with Advanced Esophageal Squamous Cell

Carcinoma (ATTRACTION-3). *Clinical Cancer Research* **28**, doi:10.1158/1078-0432.Ccr-21-0985 (2022).

17 Gao, Y. B. *et al.* Genetic landscape of esophageal squamous cell carcinoma. *Nat Genet* **46**, 1097-1102, doi:10.1038/ng.3076 (2014).

18 Song, Y. *et al.* Identification of genomic alterations in oesophageal squamous cell cancer. *Nature* **509**, 91-95, doi:10.1038/nature13176 (2014).

19 Zheng, B. *et al.* A new murine esophageal organoid culture method and organoid-based model of esophageal squamous cell neoplasia. *iScience* **24**, 103440, doi:10.1016/j.isci.2021.103440 (2021).

20 in *PDQ Cancer Information Summaries* (2002).

21 Busslinger, G. A. *et al.* Human gastrointestinal epithelia of the esophagus, stomach, and duodenum resolved at single-cell resolution. *Cell Rep* **34**, 108819, doi:10.1016/j.celrep.2021.108819 (2021).

22 Kinker, G. S. *et al.* Pan-cancer single-cell RNA-seq identifies recurring programs of cellular heterogeneity. *Nat Genet* **52**, 1208-1218, doi:10.1038/s41588-020-00726-6 (2020).

23 Popivanova, B. K. *et al.* Blockade of a chemokine, CCL2, reduces chronic colitis-associated carcinogenesis in mice. *Cancer Res* **69**, 7884-7892, doi:10.1158/0008-5472.CAN-09-1451 (2009).

24 Hao, Q., Vadgama, J. V. & Wang, P. CCL2/CCR2 signaling in cancer pathogenesis. *Cell Commun Signal* **18**, 82, doi:10.1186/s12964-020-00589-8 (2020).

25 Qian, B. Z. *et al.* CCL2 recruits inflammatory monocytes to facilitate breast-tumour metastasis. *Nature* **475**, 222-225, doi:10.1038/nature10138 (2011).

26 Tu, M. M. *et al.* Inhibition of the CCL2 receptor, CCR2, enhances tumor response to immune checkpoint therapy. *Commun Biol* **3**, 720, doi:10.1038/s42003-020-01441-y (2020).

27 Yao, J. *et al.* Single-cell transcriptomic analysis in a mouse model deciphers cell transition states in the multistep development of esophageal cancer. *Nature Communications* **11**, doi:10.1038/s41467-020-17492-y (2020).

28 Yang, H. *et al.* CCL2-CCR2 axis recruits tumor associated macrophages to induce immune evasion through PD-1 signaling in esophageal carcinogenesis. *Mol Cancer* **19**, 41, doi:10.1186/s12943-020-01165-x (2020).

29 Wu, Z. *et al.* Reprogramming of the esophageal squamous carcinoma epigenome by SOX2 promotes ADAR1 dependence. *Nat Genet* **53**, 881-894, doi:10.1038/s41588-021-00859-2 (2021).

30 Jin, J. *et al.* CCL2: An Important Mediator Between Tumor Cells and Host Cells in Tumor Microenvironment. *Front Oncol* **11**, 722916, doi:10.3389/fonc.2021.722916 (2021).

31 Ueda, A. *et al.* NF-kappa B and Sp1 regulate transcription of the human monocyte chemoattractant protein-1 gene. *J Immunol* **153**, 2052-2063 (1994).

32 Zhang, H. *et al.* B2M overexpression correlates with malignancy and immune signatures in human gliomas. *Sci Rep* **11**, 5045, doi:10.1038/s41598-021-84465-6 (2021).

33 Huang, W. C. *et al.* Novel function of THEMIS2 in the enhancement of cancer stemness and chemoresistance by releasing PTP1B from MET. *Oncogene* **41**, 997-1010, doi:10.1038/s41388-021-02136-2 (2022).

829 34 Li, S. L. *et al.* High expression of regulator of G-protein signalling 1 is associated with
830 the poor differentiation and prognosis of gastric cancer. *Oncology Letters* **21**, doi:ARTN
831 322
832 10.3892/ol.2021.12584 (2021).
833 35 Wang, V. M. *et al.* CD9 identifies pancreatic cancer stem cells and modulates glutamine
834 metabolism to fuel tumour growth. *Nat Cell Biol* **21**, 1425-1435, doi:10.1038/s41556-
835 019-0407-1 (2019).
836 36 Dasgupta, A. *et al.* Anticachectic regulator analysis reveals Perp-dependent
837 antitumorigenic properties of 3-methyladenine in pancreatic cancer. *Jci Insight* **7**,
838 doi:ARTN e153842
839 10.1172/jci.insight.153842 (2022).
840 37 Rao, X., Wang, J., Song, H. M., Deng, B. & Li, J. G. KRT15 overexpression predicts
841 poor prognosis in colorectal cancer. *Neoplasma* **67**, 410-414,
842 doi:10.4149/neo_2019_190531N475 (2020).
843 38 Turczyk, L. *et al.* Tetraspanin CD151 regulates expression of fibroblast growth factor
844 receptor-2 (FGFR2) in ductal carcinoma in situ cell line. *Eur J Cancer* **49**, S131-S131
845 (2013).
846 39 Xiao, Y., Zhu, S., Yin, W., Liu, X. F. & Hu, Y. IGFBP-4 expression is adversely
847 associated with lung cancer prognosis. *Oncology Letters* **14**, 6876-6880,
848 doi:10.3892/ol.2017.7014 (2017).
849 40 Miyake, S. *et al.* Cells degrade a novel inhibitor of differentiation with E1A-like
850 properties upon exiting the cell cycle. *Mol Cell Biol* **20**, 8889-8902, doi:Doi
851 10.1128/Mcb.20.23.8889-8902.2000 (2000).
852 41 Spranger, S. & Gajewski, T. F. Impact of oncogenic pathways on evasion of antitumour
853 immune responses. *Nat Rev Cancer* **18**, 139-147, doi:10.1038/nrc.2017.117 (2018).
854 42 Togashi, Y., Shitara, K. & Nishikawa, H. Regulatory T cells in cancer
855 immunosuppression - implications for anticancer therapy. *Nat Rev Clin Oncol* **16**, 356-
856 371, doi:10.1038/s41571-019-0175-7 (2019).
857 43 Dinh, H. Q. *et al.* Integrated single-cell transcriptome analysis reveals heterogeneity of
858 esophageal squamous cell carcinoma microenvironment. *Nat Commun* **12**, 7335,
859 doi:10.1038/s41467-021-27599-5 (2021).
860 44 Yao, J. *et al.* Single-cell transcriptomic analysis in a mouse model deciphers cell
861 transition states in the multistep development of esophageal cancer. *Nat Commun* **11**,
862 3715, doi:10.1038/s41467-020-17492-y (2020).
863 45 Fei, L., Ren, X., Yu, H. & Zhan, Y. Targeting the CCL2/CCR2 Axis in Cancer
864 Immunotherapy: One Stone, Three Birds? *Front Immunol* **12**, 771210,
865 doi:10.3389/fimmu.2021.771210 (2021).
866 46 Loyher, P. L. *et al.* CCR2 Influences T Regulatory Cell Migration to Tumors and Serves
867 as a Biomarker of Cyclophosphamide Sensitivity. *Cancer Res* **76**, 6483-6494,
868 doi:10.1158/0008-5472.CAN-16-0984 (2016).
869 47 Flores-Toro, J. A. *et al.* CCR2 inhibition reduces tumor myeloid cells and unmasks a
870 checkpoint inhibitor effect to slow progression of resistant murine gliomas. *Proc Natl*
871 *Acad Sci U S A* **117**, 1129-1138, doi:10.1073/pnas.1910856117 (2020).
872 48 Peters, W., Dupuis, M. & Charo, I. F. A mechanism for the impaired IFN-gamma
873 production in C-C chemokine receptor 2 (CCR2) knockout mice: role of CCR2 in linking

874 the innate and adaptive immune responses. *J Immunol* **165**, 7072-7077,
875 doi:10.4049/jimmunol.165.12.7072 (2000).
876 49 Miyoshi, H. & Stappenbeck, T. S. In vitro expansion and genetic modification of
877 gastrointestinal stem cells in spheroid culture. *Nat Protoc* **8**, 2471-2482,
878 doi:10.1038/nprot.2013.153 (2013).
879 50 Ko, K. P., Zhang, J. & Park, J. I. Establishing transgenic murine esophageal organoids.
880 *STAR Protoc* **3**, 101317, doi:10.1016/j.xpro.2022.101317 (2022).
881 51 Jung, Y. S. *et al.* Deregulation of CRAD-controlled cytoskeleton initiates mucinous
882 colorectal cancer via beta-catenin. *Nat Cell Biol* **20**, 1303-1314, doi:10.1038/s41556-018-
883 0215-z (2018).
884 52 Bergen, V., Lange, M., Peidli, S., Wolf, F. A. & Theis, F. J. Generalizing RNA velocity
885 to transient cell states through dynamical modeling. *Nature Biotechnology* **38**, 1408-
886 1414, doi:10.1038/s41587-020-0591-3 (2020).
887 53 Xie, Z. *et al.* Gene Set Knowledge Discovery with Enrichr. *Curr Protoc* **1**, e90,
888 doi:10.1002/cpz1.90 (2021).
889 54 Sun, D. *et al.* Identifying phenotype-associated subpopulations by integrating bulk and
890 single-cell sequencing data. *Nat Biotechnol* **40**, 527-538, doi:10.1038/s41587-021-01091-
891 3 (2022).
892 55 Van de Sande, B. *et al.* A scalable SCENIC workflow for single-cell gene regulatory
893 network analysis. *Nat Protoc* **15**, 2247-2276, doi:10.1038/s41596-020-0336-2 (2020).
894 56 Kim, M. J. *et al.* PAF remodels the DREAM complex to bypass cell quiescence and
895 promote lung tumorigenesis. *Mol Cell* **81**, 1698-1714 e1696,
896 doi:10.1016/j.molcel.2021.02.001 (2021).
897
898

Figure Legends

Extended Data 1 | Candidate genes KO in EOs. a, Oncogrids of nine candidate genes were generated based on the mutation and copy number alterations. Eighty-six patients with ESCC were analyzed from the TCGA database. **b,** Mutation types of candidate genes were analyzed in the patients' data from cBioportal and the TCGA. The genes harboring more than 50% of truncation or frameshift mutations are shown. **c,** Gene expression of FAT4 and KMT2C from ESCC patients (TCGA, n = 95) and normal (TCGA, n = 11) samples are shown with box plots. Data are shown as means ± SEM. **d,** Genetic status of each organoid line was designed as shown in the table. **e,** Bright-field images of organoids are shown. Images were taken on day 8 of passage 3. Scale bar = 50 μm. **f,** Hematoxylin-and-eosin-stained sections from KO organoids. Scale bar = 50 μm.

Fig. 1 | Genetic ablation of *Trp53* and *Notch1* induces esophageal hyperplasia and de-differentiation. a, Schematic structure of EOs. **b,** The volume of each organoid is displayed as a heatmap. **c,** H&E staining showing the structures and morphologies of each organoid. Scale bar = 50 μm. **d, e,** Organoids were stained with Mki67, Sox2, and DAPI (**d**) and the number of Mki67-stained cells was quantified (**e**). WT: *p53*$^{flox/flox}$, N: *Notch1* KO, C: *Cdkn2a* KO, CN: *Cdkn2a* KO + *Notch1* KO, P: *Trp53*$^{del/del}$, PN: *Trp53*$^{del/del}$ + *Notch1* KO, PC: *Trp53*$^{del/del}$ + *Cdkn2a* KO, PCN: *Trp53*$^{del/del}$ + *Cdkn2a* KO + *Notch1* KO. Scale bar = 20 μm. ****P < 0.0001. **f,** Trp63 staining of WT, PC, PN, and PCN organoids. Scale bar = 20 μm. **g,** BrdU-incorporated organoid cells were stained with anti-BrdU antibody, and the total cell nuclei were stained with DAPI. Scale bar = 10 μm. **h,** Number of BrdU-positive cells in an organoid of WT, PN, and PCN is shown in bar plots. ****P < 0.0001. **i,** Bright-field images of WT, PN, and PCN organotypic cultures were shown. Scale bar = 50 μm. **j,** Organotypic cultured WT, PN, and PCN cells were fixed and stained with E-cadherin. Red fluorescence was visualized to show stromal cells derived from nT-nG mice. Scale bar = 50 μm. **k, l,** Colony formation ability (**k**) and cell growth rate (**l**) of PN and PCN were evaluated at different time points.

Supplementary Fig. 1 | Establishment of CRISPR/Cas9-based KO organoids and validation. a, Representative images of mouse EO growth of *p53*$^{flox/flox}$ are shown. Images were taken from day 3 to day 9 of passage 3. Scale bar = 20 μm. **b,** KO efficiency of each sgRNA was validated with immunoblot. Three different sgRNA constructs of each gene were tested with transient transfection. **c,** Genomic DNA of each organoid was sequenced to verify CRISPR/Cas9-induced gene editing. Pink boxes show the sgRNA sequences of each gene.

Extended Data 2 | *Notch1* KO suppresses organoid differentiation and induces cell migration. a, b, Organoids were stained with Mki67, Sox2 (**a**), and Krt13 (**b**). PA: *p53*$^{del/del}$ + *Ajuba* KO, PCF4: *p53*$^{del/del}$ + *Cdkn2a* KO + *Fat4* KO, PCA: *p53*$^{del/del}$ + *Cdkn2a* KO + *Ajuba* KO, WT: *p53*$^{flox/flox}$, N: *Notch1* KO, C: *Cdkn2a* KO, CN: *Cdkn2a* KO + *Notch1* KO, and P: *Trp53*$^{del/del}$. Scale bar = 20 μm. **c,** Morphologies and internal structures of DAPT-treated P and PC organoids were compared with PN and PCN, respectively. DAPT was treated with different doses; low dose = 5 mM, high dose = 10 mM. Scale bar = 50 μm. **d,** A reversible Notch1 inhibition effect was shown in the bright-field microscopic images. Morphologies of P and PC were rescued after DAPT

942 removal in the second passage. DAPT (10 mM) was treated for 8 days for each passage. Upper
943 panel, magnification, ×50, Scale bar = 200 μm. Lower panel, magnification, ×100, Scale bar = 100
944 μm. **e,** Schematic overview of organotypic culture experiment. **f,** Bright-field images of 2D-
945 cultured cells. Images were taken on day 3 of passage 3. Scale bar = 100 μm. **g,** Wound closure
946 rates of PC, PN, and PCN cells were evaluated by analyzing images taken at 0, 8, and 20 hrs after
947 scratch with ImageJ software. **h,** Alcian Blue-PAS staining results of organoids are shown. Large
948 intestine tissue was used as a positive control. Scale bar = 50 μm.
949

950 **Fig. 2 | Single-cell transcriptomic analysis of genetically engineered esophageal organoids. a,**
951 Schematic overview of single-cell RNA-seq procedure. Four organoids (WT, PC, PN, and PCN)
952 were multiplexed for library preparation and demultiplexed after sequencing. **b, c,** UMAP of four
953 integrated datasets (WT, PC, PN, and PCN). **d,** The proportion of each cluster was compared to
954 the same cluster of the WT dataset. Cell types were annotated on the right side of the plots.
955 Statistical significance between the two groups was assessed by the permutation test. **e,** RNA
956 velocity–based UMAP projection based on the cell type in each dataset. **f,** Cell trajectory inference
957 by RNA velocity shown with streamline. **g,** A latent time analysis is shown in the velocity-based
958 UMAP. **h,** PAGA analysis of RNA velocity–based cell clusters showing the direction of cell
959 lineage on the UMAP. The size of the circle corresponds to the cell number. **i,** Representative
960 marker genes of root cell clusters are indicated with simplified lineage directions.
961

962 **Extended Data 3 | Integration and annotation of scRNA datasets of organoids. a,** Integrated
963 UMAP of WT, PC, PN, and PCN datasets (Seurat package). **b,** Heatmap of each cluster from the
964 integrated dataset. **c,** Cells were clustered by 35 subtypes and annotated as four cell types based
965 on the marker genes. **d,** Marker gene expression of each cell type shown in the dot plot. **e,** The
966 proportion comparison of each cell cluster from the PC dataset and WT.
967

968 **Fig. 3 | Transcriptomes of PN and PCN recapitulate the ESCC phenotype. a,** Dot plot showing
969 cancer stem cell marker gene expression in each cell cluster of the dataset. **b, c,** ESCC phenotype–
970 associated cells were marked as $ESCC^{+}$ cells in the Scissor-based UMAP projection (**b**), and the
971 proportion of $ESCC^{+}$ cells is shown in the bar plot (**c**). **d, e,** Poor survival of ESCC patient–
972 associated cells is displayed as Poor $survival^{+}$ cells in the UMAP (**d**), and the proportion was
973 analyzed (**e**). **f,** A gene set enrichment analysis was performed to compare the gene signature of
974 ESCC to each geneset of the PN or PCN dataset. **g,** Heatmap clustering of bulk RNA-sequencing
975 from WT, PN, and PCN organoids. **h,** An Enrichr analysis was performed with RNA-seq result.
976 PN-enriched genes or PCN-enriched genes compared to WT were analyzed using Bioplanet and
977 REACTOME databases; the TOP5 features of each database are shown. **P* value. **i,** Dot plots of
978 PN or PCN highly expressed genes were compared to the gene sets of the Kyoto Encyclopedia of
979 Genes and Genomes (KEGG) pathways. Dot size represents the gene number count, and colors
980 show the adjusted *P* value.
981

982 **Fig. 4 | *In vivo* tumorigenicity of PCN with pro-tumorigenic TME. a,** Tumor growth of PN and
983 PCN was monitored after transplantation into C57BL/6 mice. **b,** H&E staining showing tumor

984 cells and the TME. Red arrowheads, mitotic cells; black arrowhead, blood vessel; dotted circle,
985 inflammatory cells. Scale bar = 100 μm. **c,** Transplanted tumor cells were stained with ESCC
986 cancer stem cell marker Trp63 and proliferative cell marker Mki67. Scale bar = 100 μm. **d,** An
987 Enrichr analysis with a bulk RNA-seq result. DEGs were created with PCN and PN datasets, and
988 PCN highly expressed genes were input for a Reactome analysis. **e,** Volcano plot from a DEG
989 analysis of PCN and PN from a scRNA analysis. **f,** Feature plot of Ccl2 expression from WT, PN,
990 and PCN scRNA-seq results. Split UMAPs were displayed with each dataset. **g-i,** Tumor growth
991 measured in PCN and PCN-*Ccl2* KO cell–transplanted mice. **j,** Pdcd1^{+}, perforin^{+}, Cd8^{+}, Cd206^{+},
992 Cd209^{+}, and Mki67^{+} cells in randomly chosen 630× magnified images were analyzed and plotted.
993 n.s. = not significant. **k,** Pdcd1/Pd-1, perforin, Cd8, Cd206, Cd209, and Mki67 staining of PCN
994 and PCN-*Ccl2* KO–derived tumors. Scale bar = 20 μm.
995

996 **Extended Data 4 | Ccl2 relevance in immune response. a,** Tumor-infiltrated immune cells of
997 PCN-transplanted tumor tissues were stained with Havcr2/Tim3, Pdcd1/Pd-1, Cd8, Cd4, Mpo, and
998 Cd209/Dc-sign. Nuclei were stained with DAPI. Scale bar = 50 μm. Dotted circle, inflammatory
999 cells. **b,** An Enrichr analysis from PCN highly expressed genes in proliferating cells from the
1000 scRNA-seq results of PN and PCN datasets. DEGs were created between proliferating cells of
1001 PCN and PN, and the relevant pathways were analyzed with BioPlanet and the KEGG databases.
1002 **c,** An Enrichr analysis with bulk RNA-seq results. PCN highly expressed genes compared to PN
1003 were analyzed using gene ontology biological process (GOBP) database. **d,** Dot plots showing the
1004 gene expression of *Ccl2*, *Cxcl1*, and *Cxcl2* in a different cell type and datasets of organoids from
1005 scRNA-seq results. **e,** *Ccl2* expression in the PC dataset displayed on UMAP. **f,** Dot plot from
1006 scRNA-seq showing *Ccl2* gene expression in different genotypes of organoids. **g, h,** Cxcl1 and
1007 Cxcl2 gene expression in different genotypes of organoids shown on a dot plot (**g**) and UMAP (**h**).
1008 **i,** PCN-transplanted tumors were stained with Ccl2 and Ccr2 antibodies. Scale bar = 50 μm.
1009

1010 **Extended Data 5 | TME comparison of PCN- and PCN-*Ccl2* KO–transplanted tumors. a,**
1011 Sanger sequencing results of PCN and PCN-*Ccl2* KO cells. Pink box showing the sgRNA
1012 sequences for the *Ccl2* gene. **b,** Growth rates of PCN and PCN-Ccl2 KO cells. **c,** H&E staining of
1013 PCN- and PCN-*Ccl2* KO–derived tumors. Scale bar = 100 μm. **d,** Pdcd1/Pd-1, Cd8, Cd3, Cd206,
1014 Cd209, Cd68, Cd11b, Ly6g, cleaved-Caspase3 (cCas3), and Mki67 staining in PCN- and PCN-
1015 *Ccl2* KO cell–derived tumors. Samples were counterstained with DAPI. Scale bar = 100 μm. **e,**
1016 Randomly chosen 630× magnified images were analyzed and plotted. n.s. = not significant. **f,**.
1017 Higher magnification (630×) images of Cd68, Cd80, Cd11b, and Ly6g staining. Scale bar = 20
1018 μm.
1019

1020 **Fig. 5 | CCL2-CCR2-induced immune evasion during ESCC development. a,** Epithelial cells'
1021 Ccl2 expression of each disease status is shown with dot plots. **b,** Dot plot showing the Ccr2
1022 expression in each type of immune cell based on the disease status. **c,** Ligand-receptor interactions
1023 predicted between epithelial cells and immune cells (using the Squidpy package). Ccl2- and Ccr2-
1024 interacting proteins are displayed with different disease stages. **d,** Ligand-receptor interactions
1025 related to the CCL pathway were predicted in sub-clusters of immune cells and epithelial cells.
1026 CCL pathway-related ligand-receptor interactions at different disease status (normal, hyperplasia,

1027 and cancer in situ) were calculated and visualized with the circle plot using the CellChat package.
1028 **e,** Significant interactions of the CCL pathway in epithelial cells with T_{ex} cell, MDSC, and
1029 macrophage sub-clusters were plotted using a chord diagram. The predicted genes were annotated.
1030 Directions from the ligand (epithelial cell) to the receptor (immune cell) are indicated. **f,** Tumors
1031 from Sox2-overexpressed PCN (PCNS) cell–transplanted mice were monitored and measured after
1032 injection of Ccr2 inhibitors (Ccr2 22 and BMS-813160). DMSO was used as vehicle control.
1033 Reagents were intraperitoneally injected three times on days 17, 21, and 25. ***$P < 0.001$, ****P
1034 < 0.0001. **g, h,** Vehicle-, Ccr2 22-, and BMS-813160-treated tumors were stained with Pdcd1/Pd-
1035 1, perforin, Cd8, and Cd206 antibodies (**h**), and the results were analyzed (**g**). Scale bar = 20 μm,
1036 *$P < 0.05$, **$P < 0.01$, ***$P < 0.001$, ****$P < 0.0001$, n.s. = not significant.
1037

1038 **Extended Data 6 | Unsupervised clustering and annotation of epithelial cells and immune**
1039 **cells of mouse ESCC model datasets. a,** Heatmap showing the marker genes of each cluster of
1040 epithelial cells. **b,** scRNA-seq data of 4-NQO-treated mouse esophagus epithelial cells were
1041 projected with UMAP and clustered by disease status. Normal: 0 week of 4-NQO treatment,
1042 inflammation: 12 weeks of 4-NQO treatment, hyperplasia: 20 weeks of 4-NQO treatment,
1043 dysplasia: 22 weeks of 4-NQO treatment, cancer *in situ*: 24 weeks of 4-NQO treatment, invasive
1044 cancer: 26 weeks of 4-NQO treatment. **c,** UMAP projection of cells with cell type annotations
1045 based on the marker gene expression. **d,** Heatmap showing the marker genes of the immune cell
1046 sub-clusters. **e,** Immune cells of each disease status are clustered by cell types and displayed with
1047 UMAP. **f,** Detailed sub-clusters of immune cells are annotated by marker gene expression using
1048 the CellKb database.
1049

1050 **Extended Data 7 | Ccl2-Ccr2 interaction in epithelial and immune cells of the mouse ESCC**
1051 **model. a,** Trp53, Cdkn2a, and Notch signaling pathway genes expression were displayed at the
1052 different disease stages after 4-NQO treatment by dot plot. **b,** ESCC patients-associated cells were
1053 assessed using the Scissor package and displayed with red dots in the UMAP. Blue dots represent
1054 normal cell-associated cells, and gray dots are background cells. **c,** ESCC-associated cell
1055 proportions of each disease status are displayed with bar plots. **d, e,** Feature plot (**d**) and dot plot
1056 (**e**) of Ccr2 expression in immune cells. Plots were visualized on the basis of the disease status. **f,**
1057 Ccr2 expression displayed in the dot plot for the sub-clusters of T cells. **g,** T_{ex} cell marker gene
1058 expression in the immune cell clusters were displayed with a dot plot. **h,** Ligand-receptor
1059 interactions related to the CCL pathway were predicted in sub-clusters of immune cells and
1060 epithelial cells. Interactions in the CCL pathway in each disease status (inflammation, dysplasia,
1061 and invasive cancer) were calculated and visualized with the circle plot. **i,** Significant interactions
1062 of the CCL pathway in epithelial cells with T_{ex} cell, MDSC, and macrophage sub-clusters were
1063 plotted in inflammation, dysplasia, and invasive cancer status using a chord diagram. The predicted
1064 genes were annotated for ligands in epithelial cells and receptors in immune cells.
1065

1066 **Extended Data 8 | Immune landscape regulation by Ccr2 inhibitors during tumorigenesis. a,**
1067 qRT-PCR results showing the relative mRNA expression of Ccl2 in PCN and Sox2-overexpressed
1068 PCN (PCNS) cells. n.s. = not significant. **b, c,** Tumorigenicity comparison in PCN and PCNS cells.
1069 **d,** Cell growth of PCNS was assessed after treatment with DMSO or 1 μM of Ccr2 inhibitors (Ccr2

22 and BMS-813160) by measuring the cell number. **e,** H&E staining of vehicle-, Ccr2 22-, and BMS-813160-treated tumors. **f,** Pdcd1/Pd-1, Cd8, Mki67, Cd206, Cd68, and Cd209 staining images in vehicle-, Ccr2 22-, and BMS-813160-treated tumors. Scale bar = 100 μm. **g, h,** Images of high magnification (630×) from Cd8 and Cd209 staining results in vehicle-, Ccr2 22-, and BMS-813160-treated tumors (**g**) and quantitation of $Cd209^{+}$ cells (**h**). Scale bar = 20 μm. $^{**}P < 0.01$, n.s. = not significant.

Extended Data 9 | Rela/NF-κB is an upstream regulator of *Ccl2*. a, Venn diagram showing the overlapped transcription factors of the UCSC ChIP seq database-, PN-, and PCN-specific regulons. **b,** Schematic representation of human CCL2 promoter binding sites and transcription factors predicted in PCN regulons. **c,** Rela regulon projection in the regulon-based UMAP of WT, PC, and PCN datasets. The color shows the regulon specificity score of the cells. **d,** Network analysis of transcription factors related to human Ccl2 gene expression. Target genes of transcription factors were refined by iRegulon, and the Ccl2 connection to Taf1 and Rela was displayed. **e,** Rela immunofluorescence images of 2D-cultured PN and PCN. Nuclei were stained with DAPI. Scale bar = 10 μm. The proportion of cells with nuclear-accumulated Rela was evaluated in PN and PCN cells. **f,** qRT-PCR results showing Ccl2 expression in the PCN cells treated with different doses of NF-κB inhibitor for 6 hrs. **g,** ChIP assays showing binding activity of Rela to Ccl2 promoter in PN and PCN cells. Putative Rela binding sites (a, b, and c) and non-binding sites in the distant region (d) were analyzed with eluted DNA fragment amplification by PCR. **h,** Human ESCC tissue microarray slides from 112 samples were stained with RELA and CCL2 antibodies. Scale bar = 50 μm (lower magnification) and 20 μm (higher magnification). **i,** Correlations between RELA and CCL2 are displayed with a heatmap. The Pearson correlation coefficient (r) and *P* value (*p*) are displayed. *n* = number of samples.

Fig. 6 | Classification of ESCC patients and PCN relevance. a, Tumor epithelial cells of 69 ESCC patients were integrated with PCN organoid cells and displayed with UMAP. **b,** Correlation matrix heatmap of ESCC patients and PCN-integrated datasets. The dendrogram showing the distance of each dataset on the basis of principal component analysis, and the Pearson correlation is displayed with a color spectrum. Groups of patients were categorized by dendrogram and correlation. Pathway scores of TP53, CDKN2A, and NOTCH were displayed on the top. PCN was excluded for pathway scores. **c,** UMAP showing each group of patients and PCN dataset. **d,** Pathway scores of TP53, CDKN2A, and NOTCH were displayed in each group of patients using a dot plot. **e,** Dot plot showing the NF-κB score genes in each group of patients. **f,** CCL2**,** Cd274 (PD-L1) and PDCD1LG2 (PD-L2) gene expression in each group of patients. **g,** Representative marker gene expressions of each group were visualized in each patient. Genes were selected from the DEG analysis using the Wilcoxon method. **h, i,** B2M and CCL2 staining results from human ESCC tissue microarray samples (**h**) and the correlation of the results (**i**). Scale bar = 50 μm (lower magnification) and 20 μm (higher magnification). Pearson correlation coefficient (r) and *P* value (p) are displayed. *n* = number of samples. **j, k,** Heatmap of B2M staining results in tumor samples (**j**) and B2M, CCL2, and RELA staining results in ESCC patients with adjacent normal and tumor paired samples (**k**). IHC scores displayed from 1 (lowest expression) to 3 (highest expression).

1113 **Extended Data 10 | Characterization of ESCC patient subgroups. a,** CD274 (PD-L1)
1114 expression in each patient shown with a dot plot. **b,** Stacked bar plot with each group of patients
1115 and their tumor grade. **c,** Expression of marker genes of each patient group. **d,** Expression of
1116 marker genes from each group was assessed by survival duration. A Kaplan-Meier plot was drawn
1117 by splitting ESCC patients from the TCGA database by the median value of each gene expression.
1118 **e,** Expression levels of marker genes of each group were measured in ESCC patients of the TCGA
1119 database and shown with box plots. NT: normal tissue of EAC and ESCC, TP: tumor from ESCC
1120 patients. **f,** Heatmap display of the correlation matrix of human ESCC tissue microarray sample
1121 staining results of B2M, CCL2, and RELA.

Extended Data 1

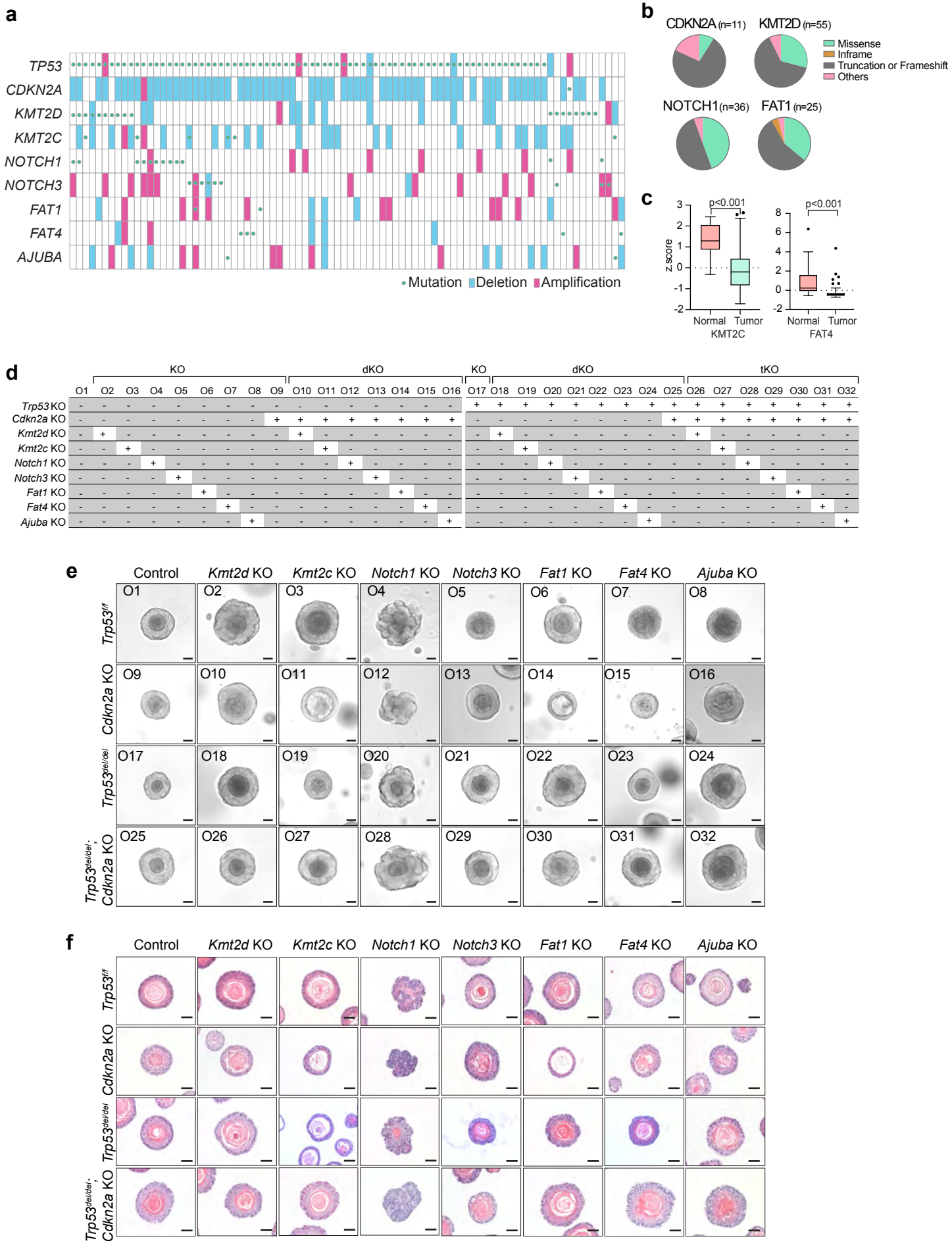

Figure 1

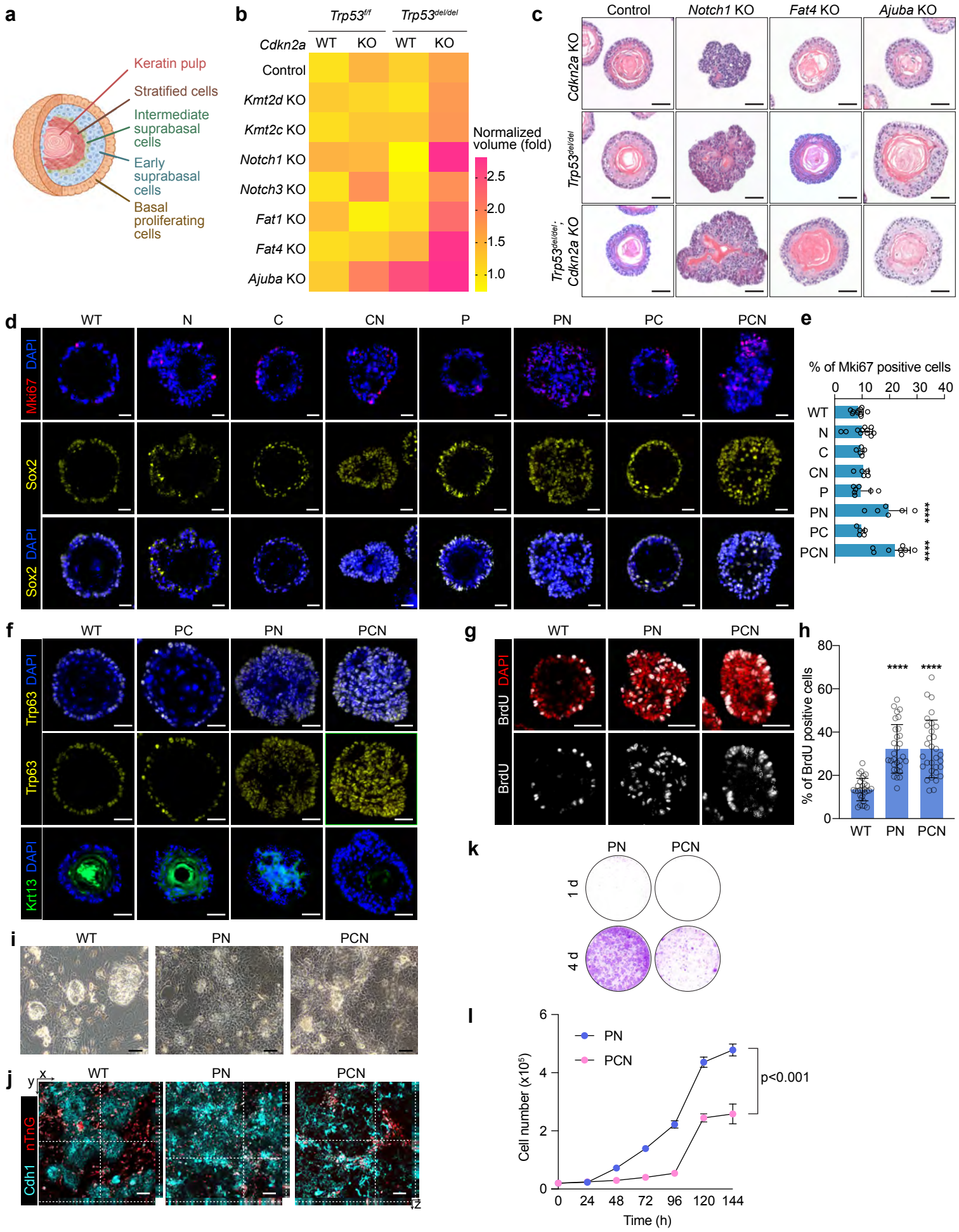
a
Keratin pulp
Stratified cells
Intermediate suprabasal cells
Early suprabasal cells
Basal proliferating cells
b
Trp53f/f
Trp53del/del
Cdkn2a
WT
KO
WT
KO
Control
Kmt2d KO
Kmt2c KO
Notch1 KO
Notch3 KO
Fat1 KO
Fat4 KO
Ajuba KO
Normalized volume (fold)
2.5
2.0
1.5
1.0
c
Control
Notch1 KO
Fat4 KO
Ajuba KO
Cdkn2a KO
Trp53del/del
Trp53del/del ; Cdkn2a KO
d
WT
N
C
CN
P
PN
PC
PCN
Mki67
DAPI
Sox2
Sox2
DAPI
e
% of Mki67 positive cells
0
10
20
30
40
WT
N
C
CN
P
PN
PC
PCN
****
****
f
WT
PC
PN
PCN
Trp63
DAPI
Trp63
Krt13
DAPI
g
WT
PN
PCN
BrdU
DAPI
BrdU
h
% of BrdU positive cells
80
60
40
20
0
****
****
WT
PN
PCN
i
WT
PN
PCN
j
x
y
z
WT
PN
PCN
nTnG
Cdh1
k
PN
PCN
1 d
4 d
l
Cell number (x10^5)
6
4
2
0
PN
PCN
p<0.001
0
24
48
72
96
120
144
Time (h)

Supplementary Figure 1

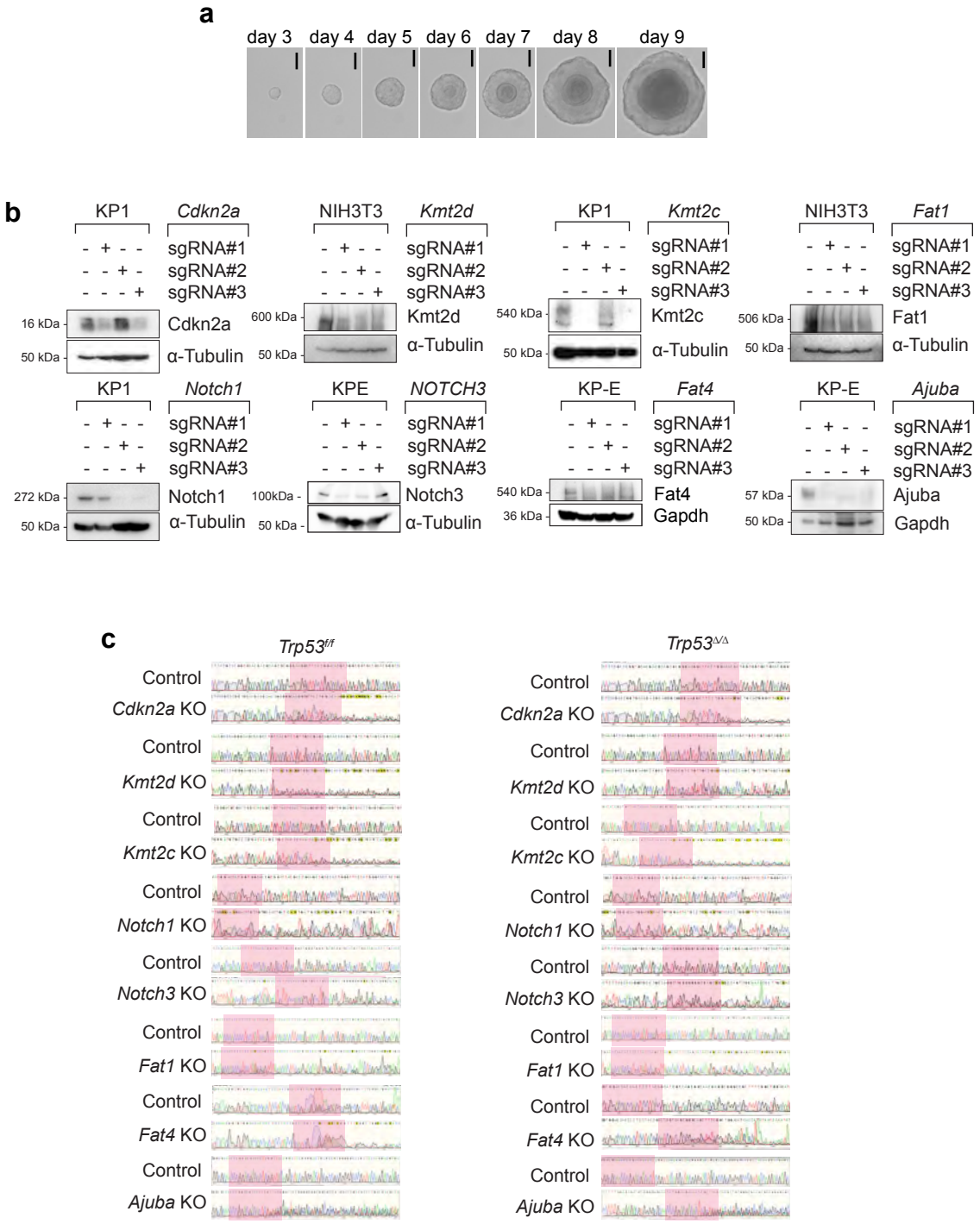

Extended Data 2

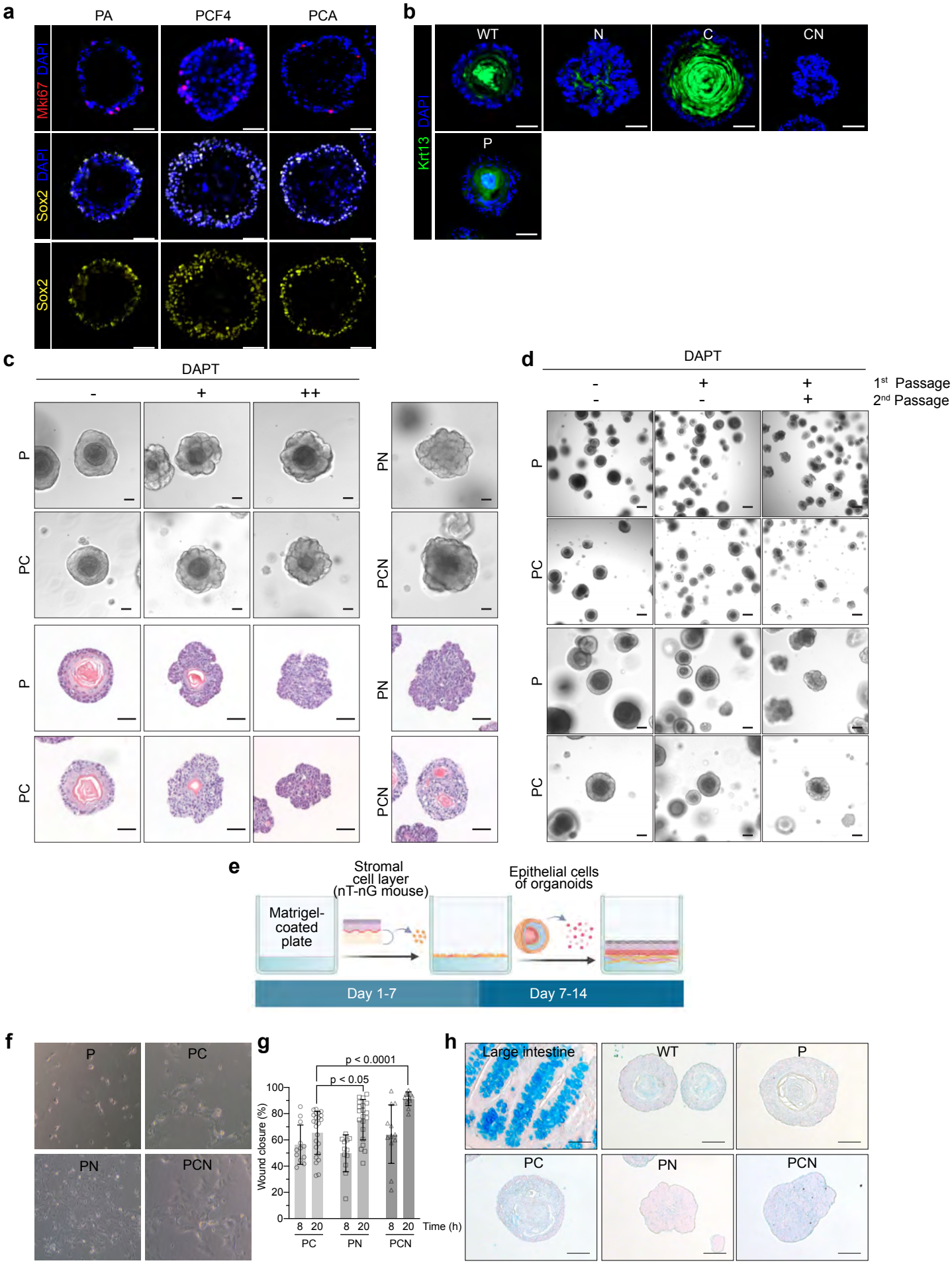

Figure 2

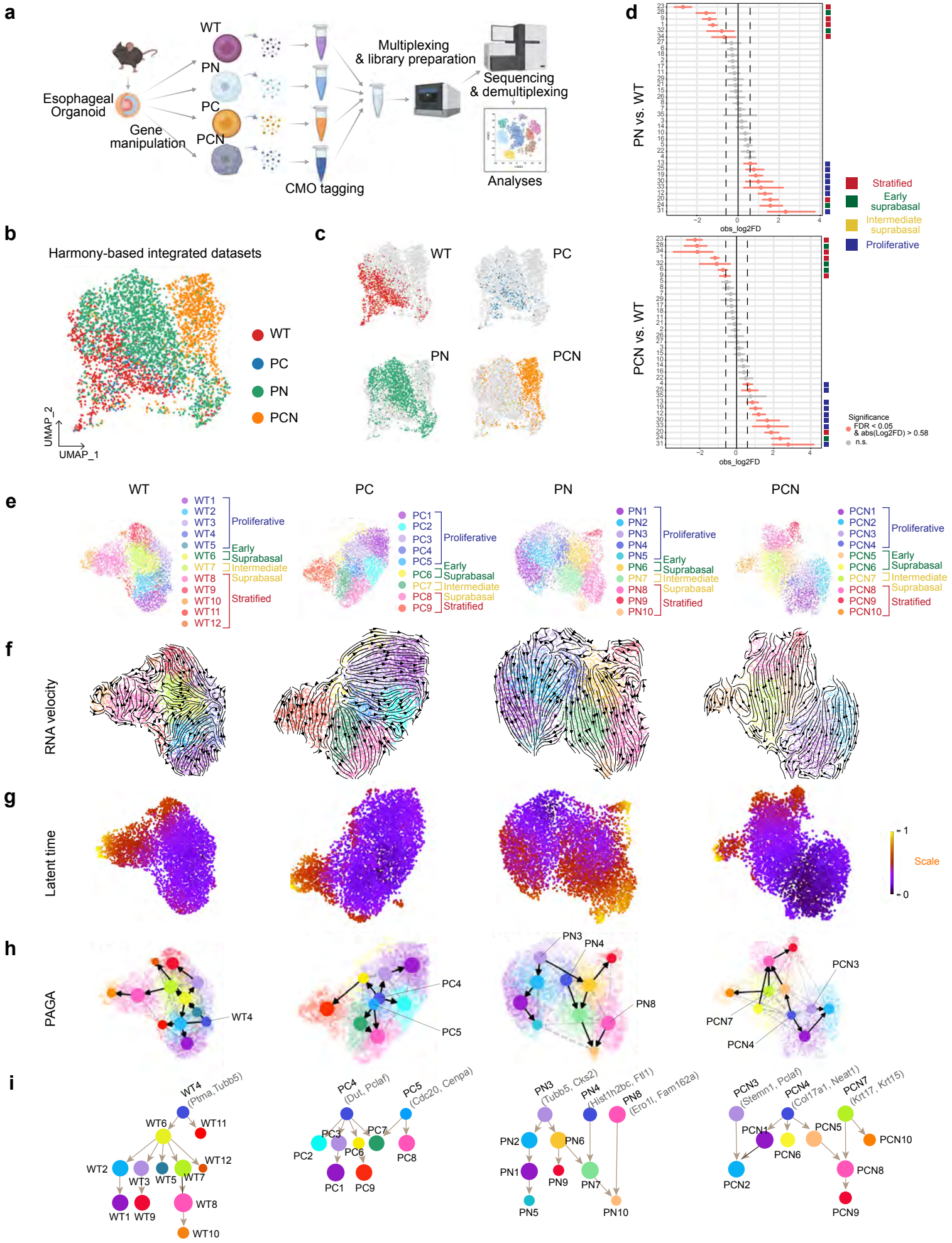
a
Esophageal Organoid
Gene manipulation
WT
PN
PC
PCN
CMO tagging
Multiplexing & library preparation
Sequencing & demultiplexing
Analyses
b
Harmony-based integrated datasets
WT
PC
PN
PCN
UMAP_2
UMAP_1
c
WT
PC
PN
PCN
d
PN vs. WT
PCN vs. WT
obs_log2FD
Stratified
Early suprabasal
Intermediate suprabasal
Proliferative
Significance
FDR < 0.05 & abs(Log2FD) > 0.58
n.s.
e
WT
PC
PN
PCN
Proliferative
Early Suprabasal
Intermediate Suprabasal
Stratified
f
RNA velocity
g
Latent time
Scale
h
PAGA
WT4
PC4
PC5
PN3
PN4
PN8
PCN3
PCN7
PCN4
i
WT4 (Ptma, Tubb5)
WT6
WT11
WT2
WT3
WT5
WT7
WT12
WT8
WT1
WT9
WT10
PC4 (Dut, Pclaf)
PC5 (Cdc20, Cenpa)
PC3
PC7
PC2
PC6
PC8
PC1
PC9
PN3 (Tubb5, Cks2)
PN4 (Hist1h2bc, Ftl1)
PN8 (Ero1l, Fam162a)
PN2
PN6
PN1
PN9
PN7
PN5
PN10
PCN3 (Stemn1, Pclaf)
PCN4 (Col17a1, Neat1)
PCN7 (Krt17, Krt15)
PCN1
PCN5
PCN10
PCN6
PCN8
PCN2
PCN9

Extended Data 3

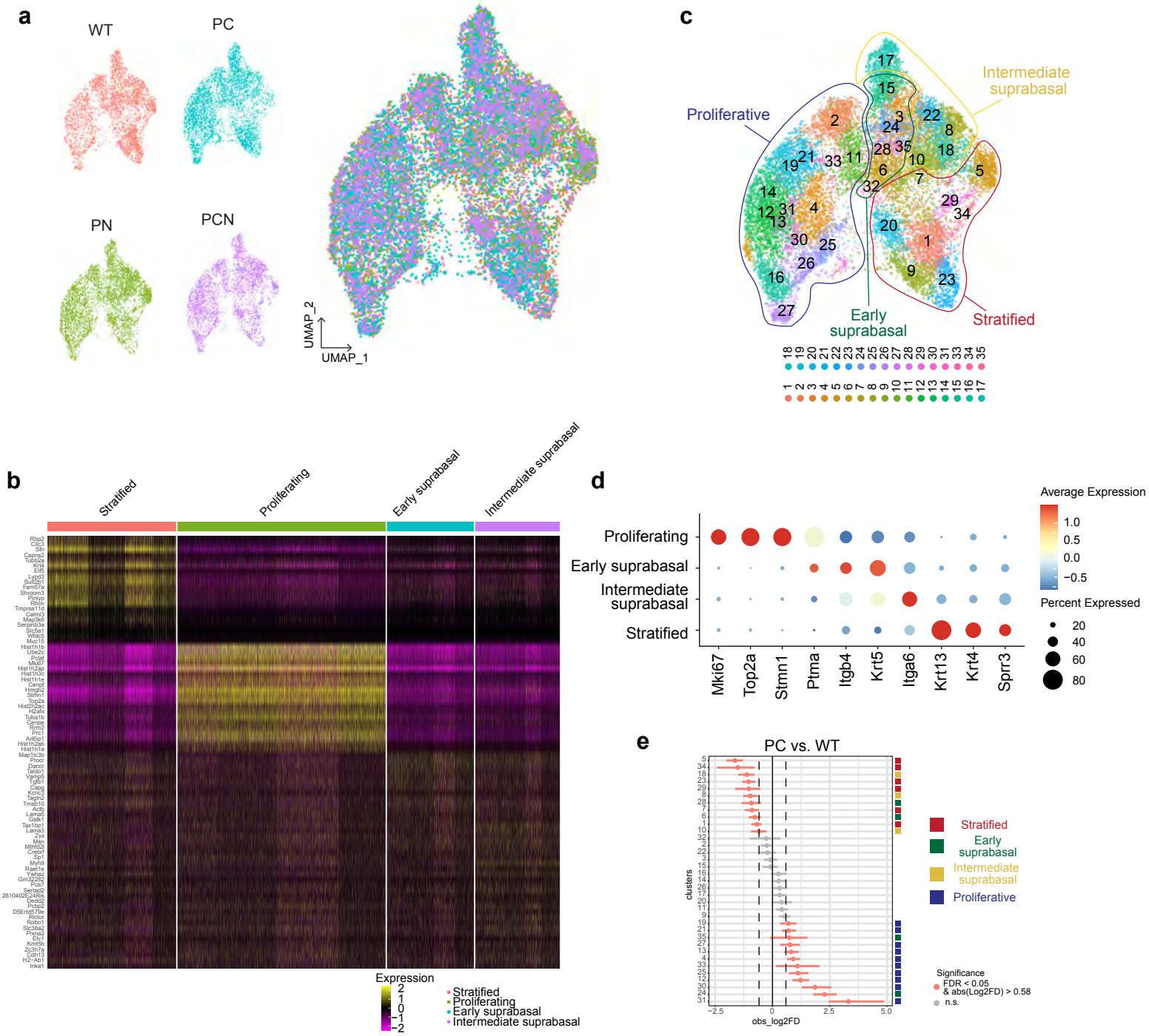

Figure 3

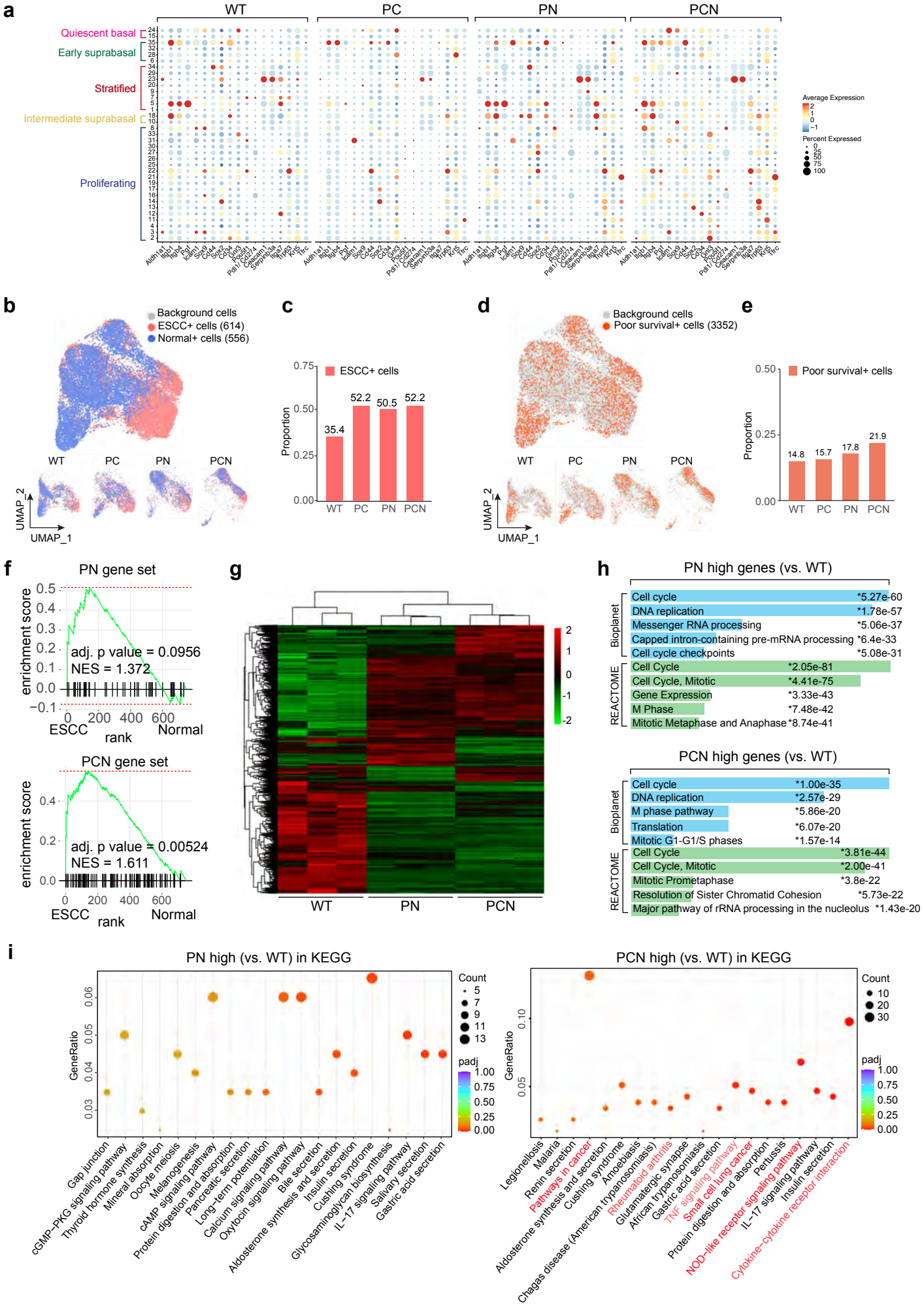
a
WT
PC
PN
PCN
Quiescent basal
Early suprabasal
Stratified
Intermediate suprabasal
Proliferating
Average Expression
Percent Expressed
b
Background cells
ESCC+ cells (614)
Normal+ cells (556)
UMAP_1
UMAP_2
c
ESCC+ cells
Proportion
35.4
52.2
50.5
52.2
d
Background cells
Poor survival+ cells (3352)
e
Poor survival+ cells
14.8
15.7
17.8
21.9
f
PN gene set
enrichment score
adj. p value = 0.0956
NES = 1.372
ESCC
rank
Normal
PCN gene set
adj. p value = 0.00524
NES = 1.611
g
h
PN high genes (vs. WT)
Bioplanet
Cell cycle *5.27e-60
DNA replication *1.78e-57
Messenger RNA processing *5.06e-37
Capped intron-containing pre-mRNA processing *6.4e-33
Cell cycle checkpoints *5.08e-31
REACTOME
Cell Cycle *2.05e-81
Cell Cycle, Mitotic *4.41e-75
Gene Expression *3.33e-43
M Phase *7.48e-42
Mitotic Metaphase and Anaphase *8.74e-41
PCN high genes (vs. WT)
Cell cycle *1.00e-35
DNA replication *2.57e-29
M phase pathway *5.86e-20
Translation *6.07e-20
Mitotic G1-G1/S phases *1.57e-14
Cell Cycle *3.81e-44
Cell Cycle, Mitotic *2.00e-41
Mitotic Prometaphase *3.8e-22
Resolution of Sister Chromatid Cohesion *5.73e-22
Major pathway of rRNA processing in the nucleolus *1.43e-20
i
PN high (vs. WT) in KEGG
GeneRatio
Count
padj
Gap junction
cGMP-PKG signaling pathway
Thyroid hormone synthesis
Mineral absorption
Oocyte meiosis
Melanogenesis
cAMP signaling pathway
Protein digestion and absorption
Pancreatic secretion
Long-term potentiation
Calcium signaling pathway
Oxytocin signaling pathway
Bile secretion
Aldosterone synthesis and secretion
Insulin secretion
Cushing syndrome
Glycosaminoglycan biosynthesis
IL-17 signaling pathway
Salivary secretion
Gastric acid secretion
PCN high (vs. WT) in KEGG
Legionellosis
Malaria
Renin secretion
Pathways in cancer
Aldosterone synthesis and secretion
Cushing syndrome
Amoebiasis
Rheumatoid arthritis
Chagas disease (American trypanosomiasis)
Glutamatergic synapse
African trypanosomiasis
Gastric acid secretion
TNF signaling pathway
Small cell lung cancer
Protein digestion and absorption
Pertussis
NOD-like receptor signaling pathway
IL-17 signaling pathway
Insulin secretion
Cytokine-cytokine receptor interaction

Figure 4

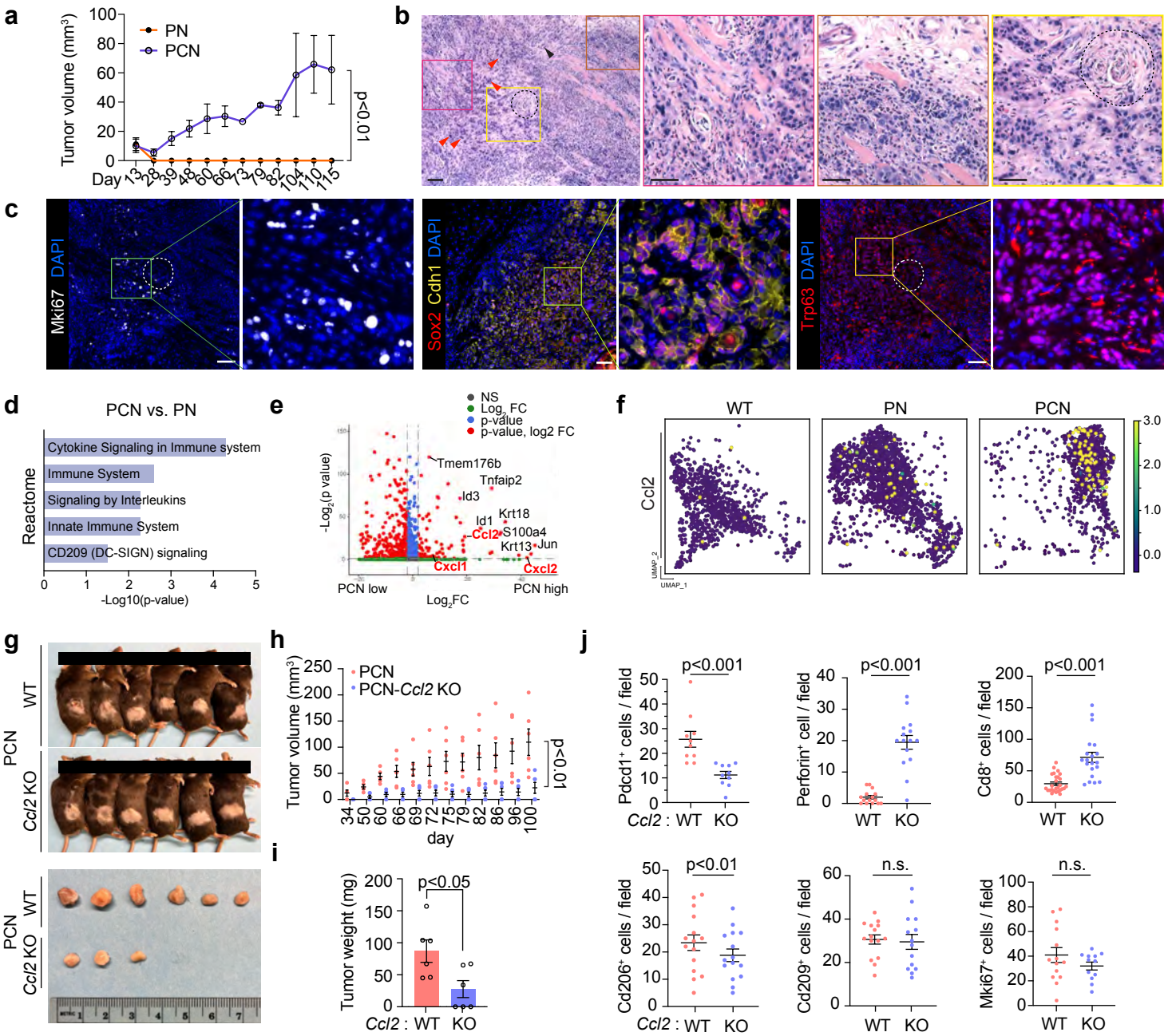
a
Tumor volume (mm³)
PN
PCN
p<0.01
Day
b
c
Mki67 DAPI
Sox2 Cdh1 DAPI
Trp63 DAPI
d
PCN vs. PN
Reactome
Cytokine Signaling in Immune system
Immune System
Signaling by Interleukins
Innate Immune System
CD209 (DC-SIGN) signaling
-Log10(p-value)
e
NS
Log2 FC
p-value
p-value, log2 FC
-Log2(p value)
Tmem176b
Tnfaip2
Id3
Krt18
Id1
Ccl2
S100a4
Krt13
Jun
Cxcl1
Cxcl2
PCN low
PCN high
Log2FC
f
WT
PN
PCN
Ccl2
UMAP_1
UMAP_2
g
PCN
WT
Ccl2 KO
h
PCN
PCN-Ccl2 KO
Tumor volume (mm³)
p<0.01
day
i
Tumor weight (mg)
p<0.05
Ccl2 : WT KO
j
Pdcd1⁺ cells / field
Perforin⁺ cell / field
Cd8⁺ cells / field
Cd206⁺ cells / field
Cd209⁺ cells / field
Mki67⁺ cells / field
p<0.001
p<0.01
n.s.
Ccl2 : WT KO
k
Pdcd1/Pd-1 DAPI
Perforin DAPI
Cd8 DAPI
Cd206 DAPI
Cd209 DAPI
Mki67 DAPI
PCN
PCN-Ccl2 KO

Extended Data 4

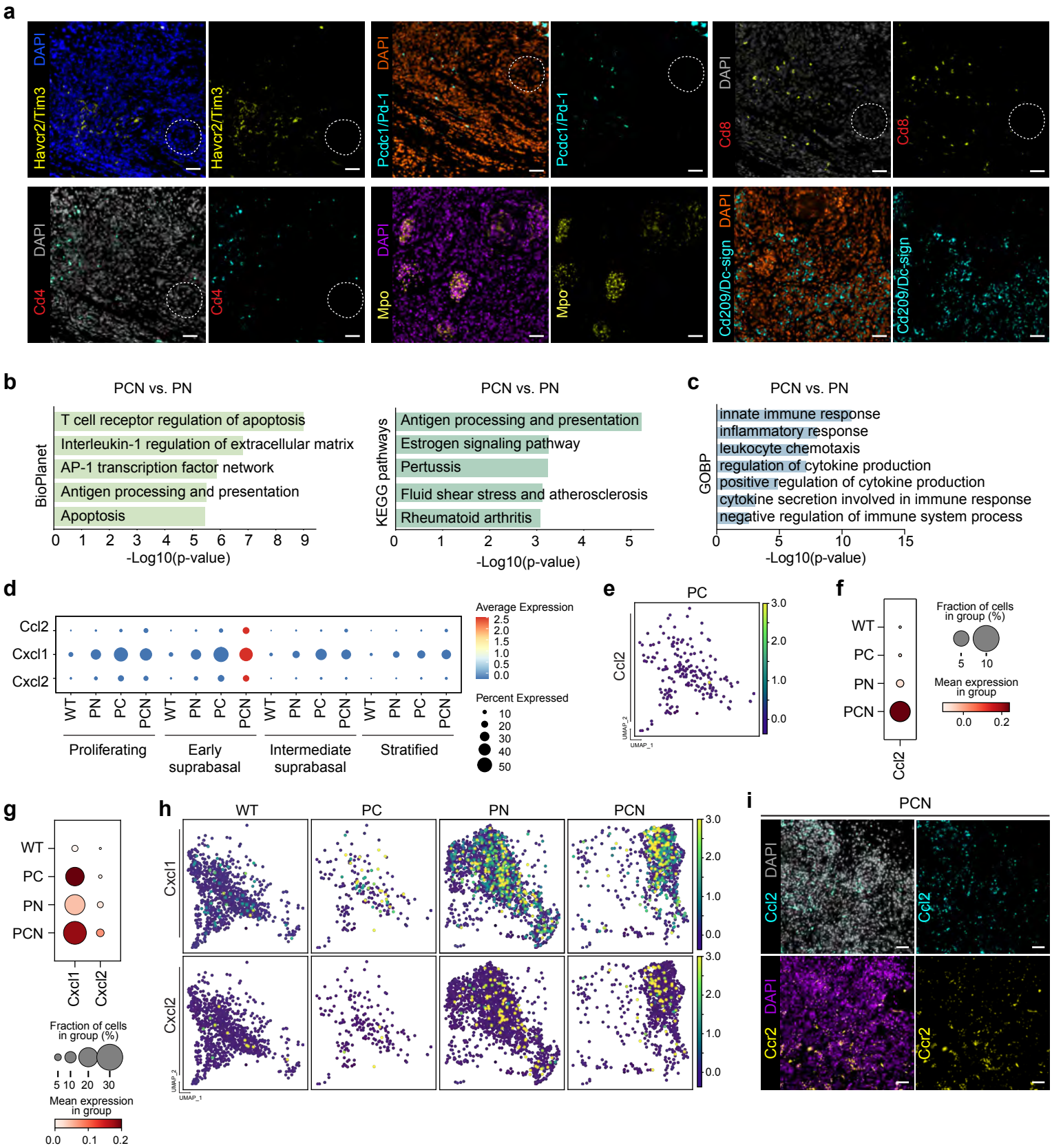

Extended Data 5

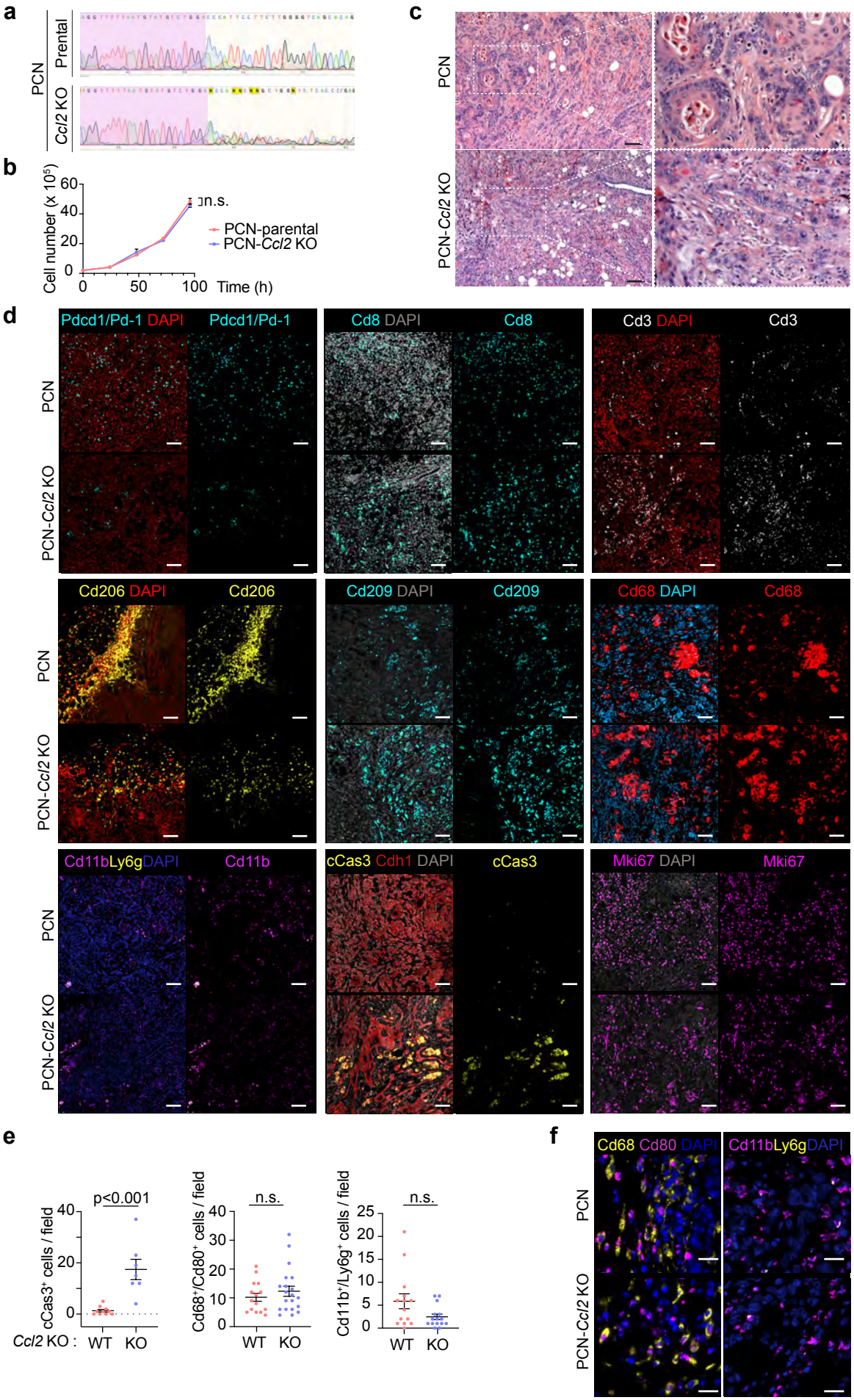

Figure 5

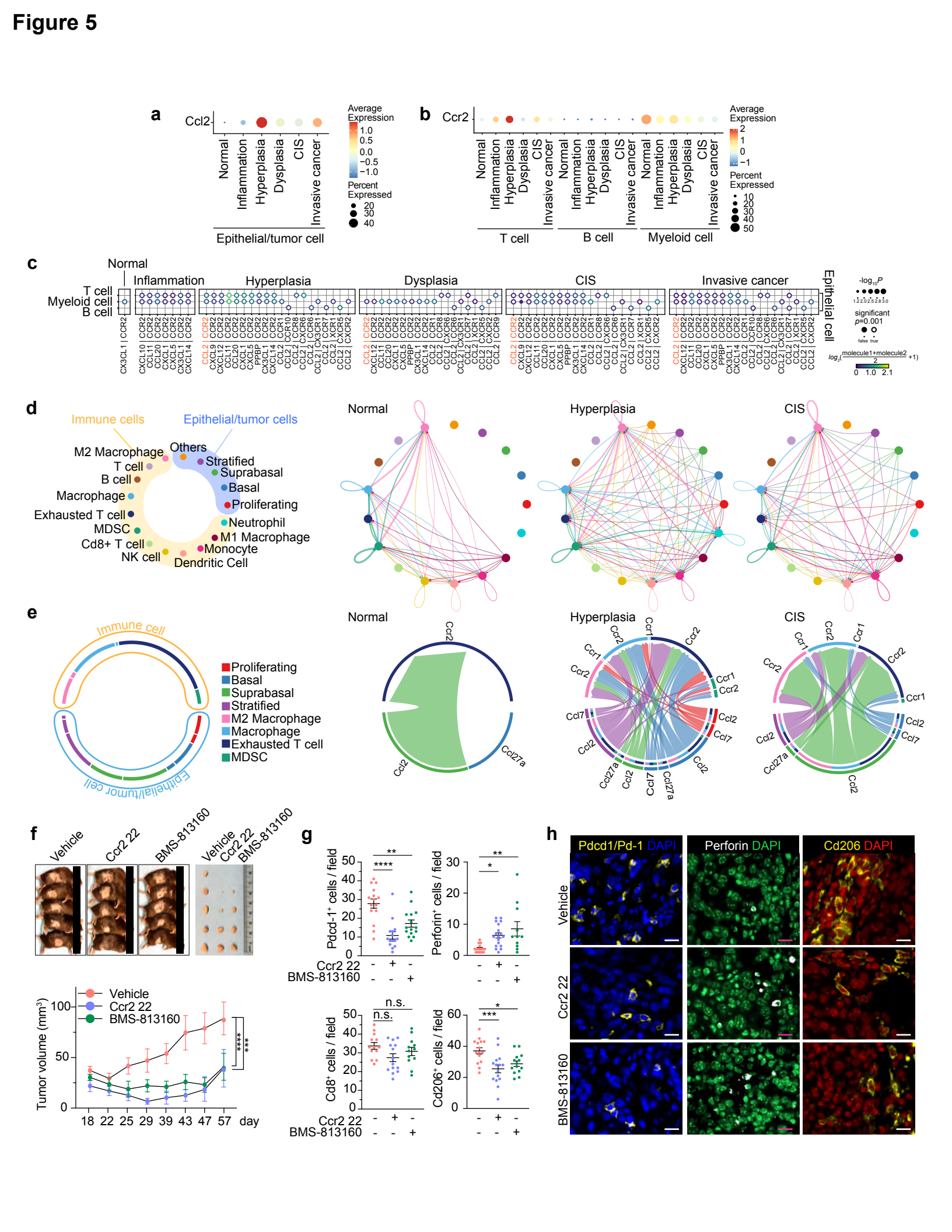
a
Ccl2
Normal
Inflammation
Hyperplasia
Dysplasia
CIS
Invasive cancer
Epithelial/tumor cell
Average Expression
Percent Expressed
b
Ccr2
T cell
B cell
Myeloid cell
c
Normal
Inflammation
Hyperplasia
Dysplasia
CIS
Invasive cancer
T cell
Myeloid cell
B cell
Epithelial cell
significant
p=0.001
d
Immune cells
Epithelial/tumor cells
M2 Macrophage
Others
T cell
B cell
Macrophage
Exhausted T cell
MDSC
Cd8+ T cell
NK cell
Dendritic Cell
Stratified
Suprabasal
Basal
Proliferating
Neutrophil
M1 Macrophage
Monocyte
Normal
Hyperplasia
CIS
e
Immune cell
Epithelial/tumor cell
Proliferating
Basal
Suprabasal
Stratified
M2 Macrophage
Macrophage
Exhausted T cell
MDSC
Normal
Hyperplasia
CIS
f
Vehicle
Ccr2 22
BMS-813160
Tumor volume (mm³)
day
g
Pdcd-1⁺ cells / field
Perforin⁺ cells / field
Cd8⁺ cells / field
Cd206⁺ cells / field
n.s.
h
Pdcd1/Pd-1 DAPI
Perforin DAPI
Cd206 DAPI
Vehicle
Ccr2 22
BMS-813160

Extended Data 6

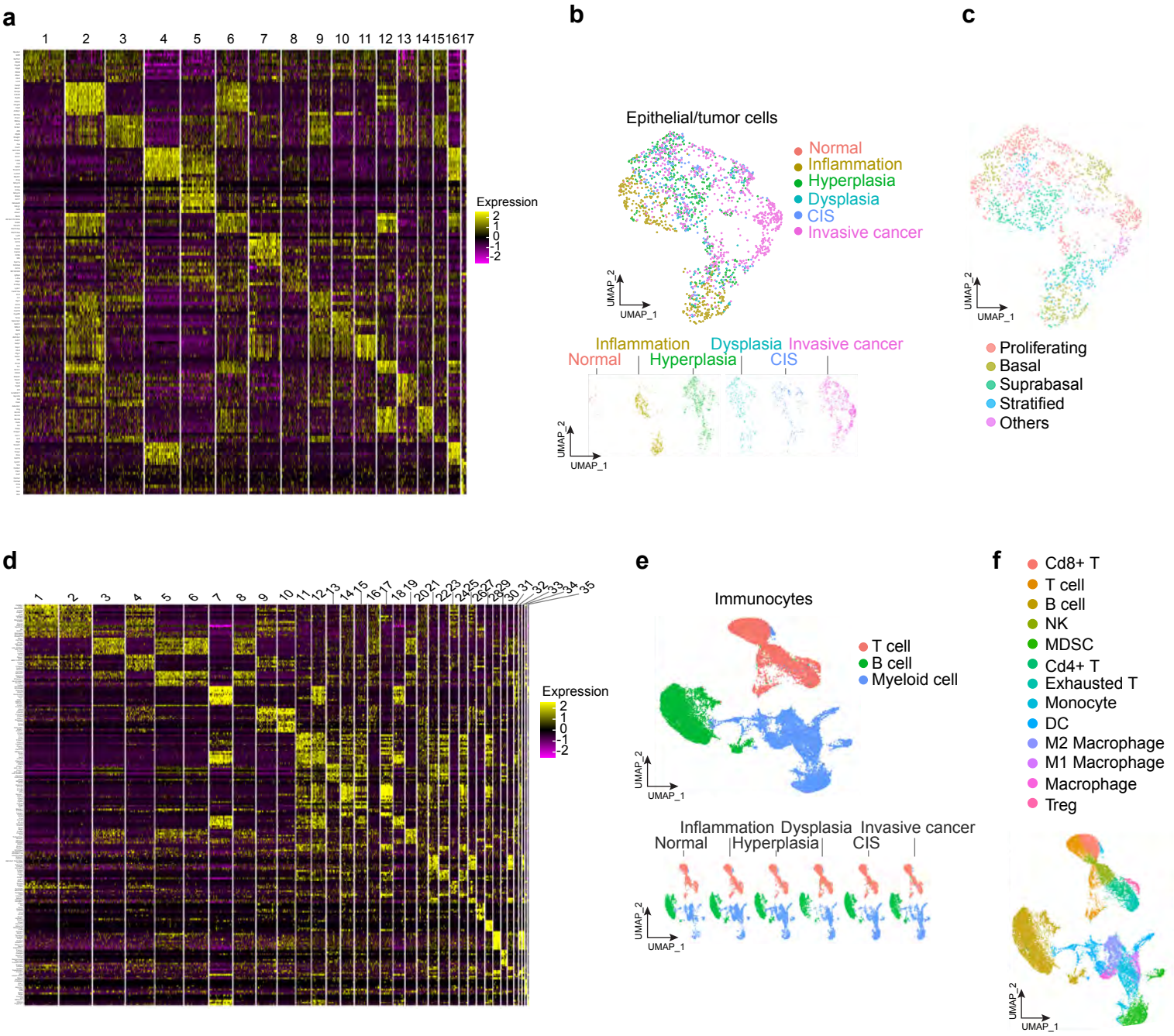

Extended Data 7

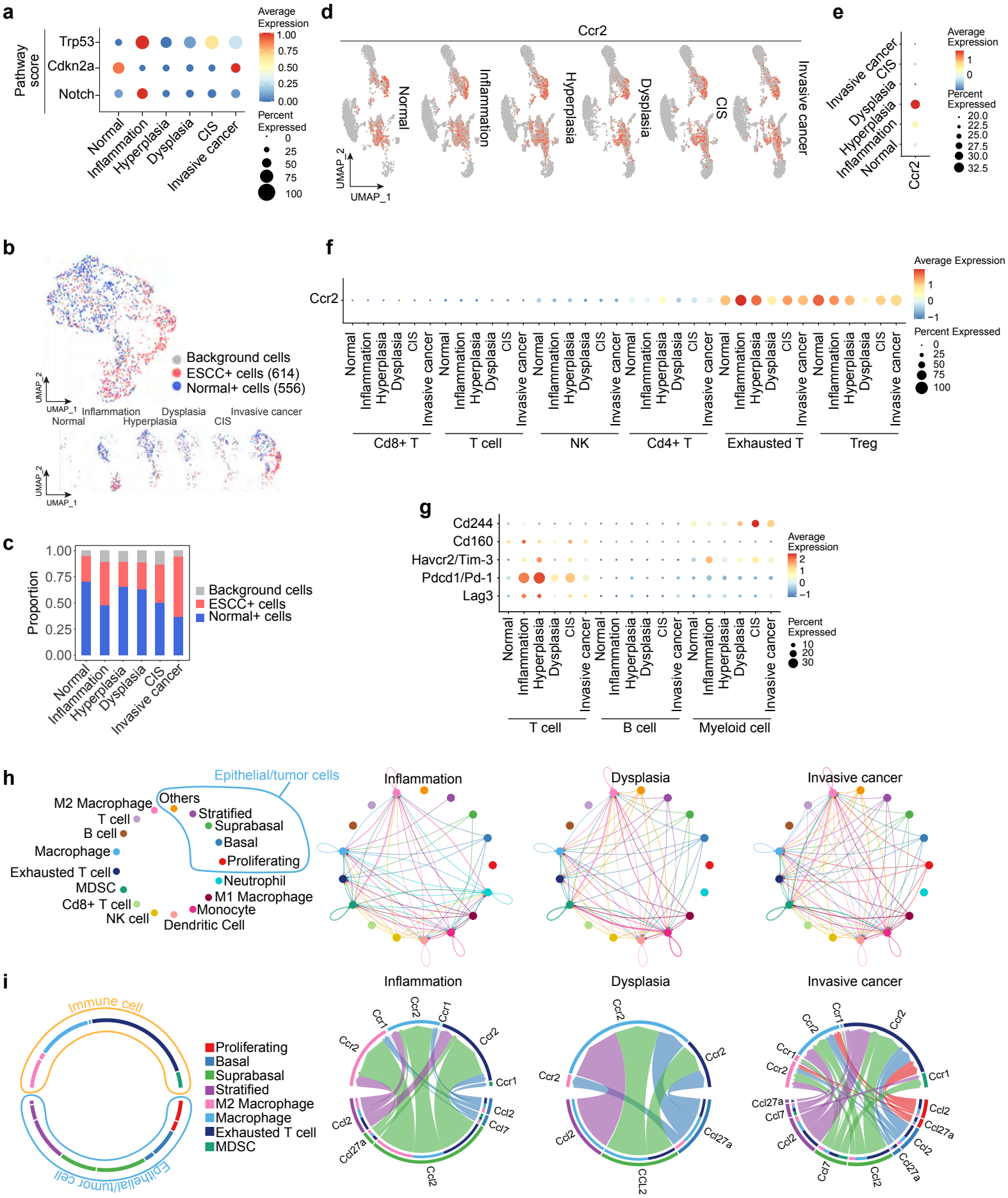

Extended Data 8

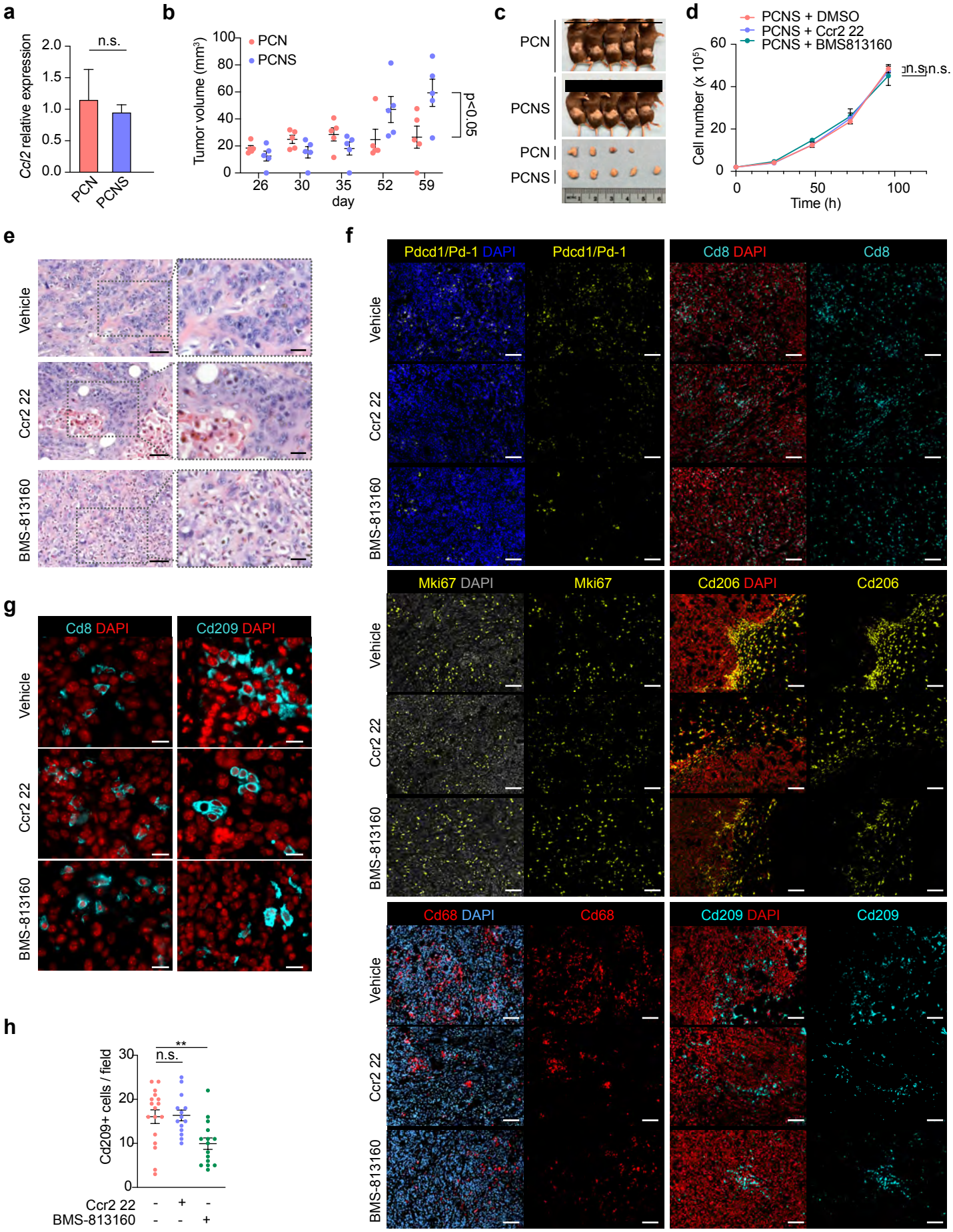

Extended Data 9

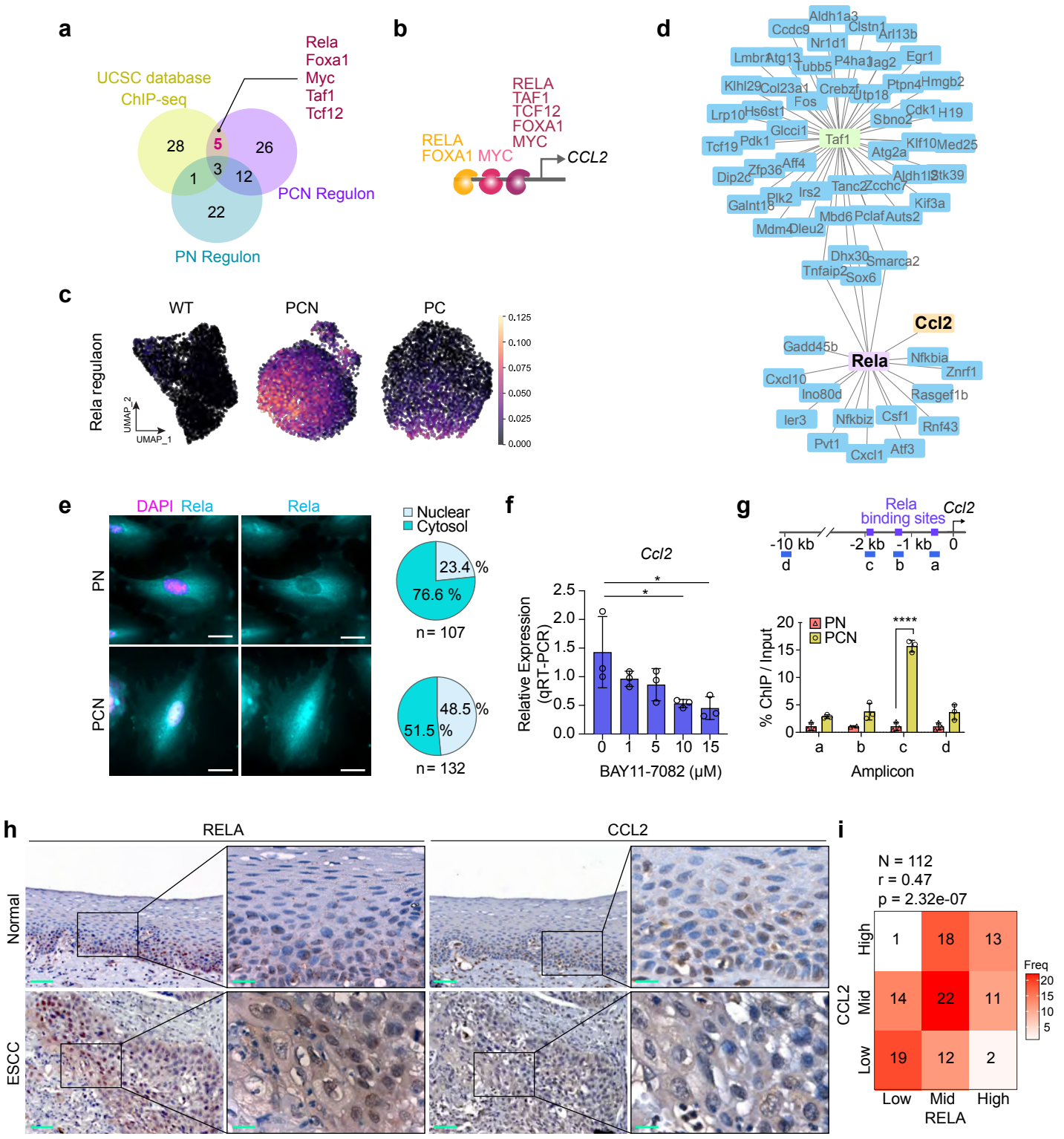

Figure 6

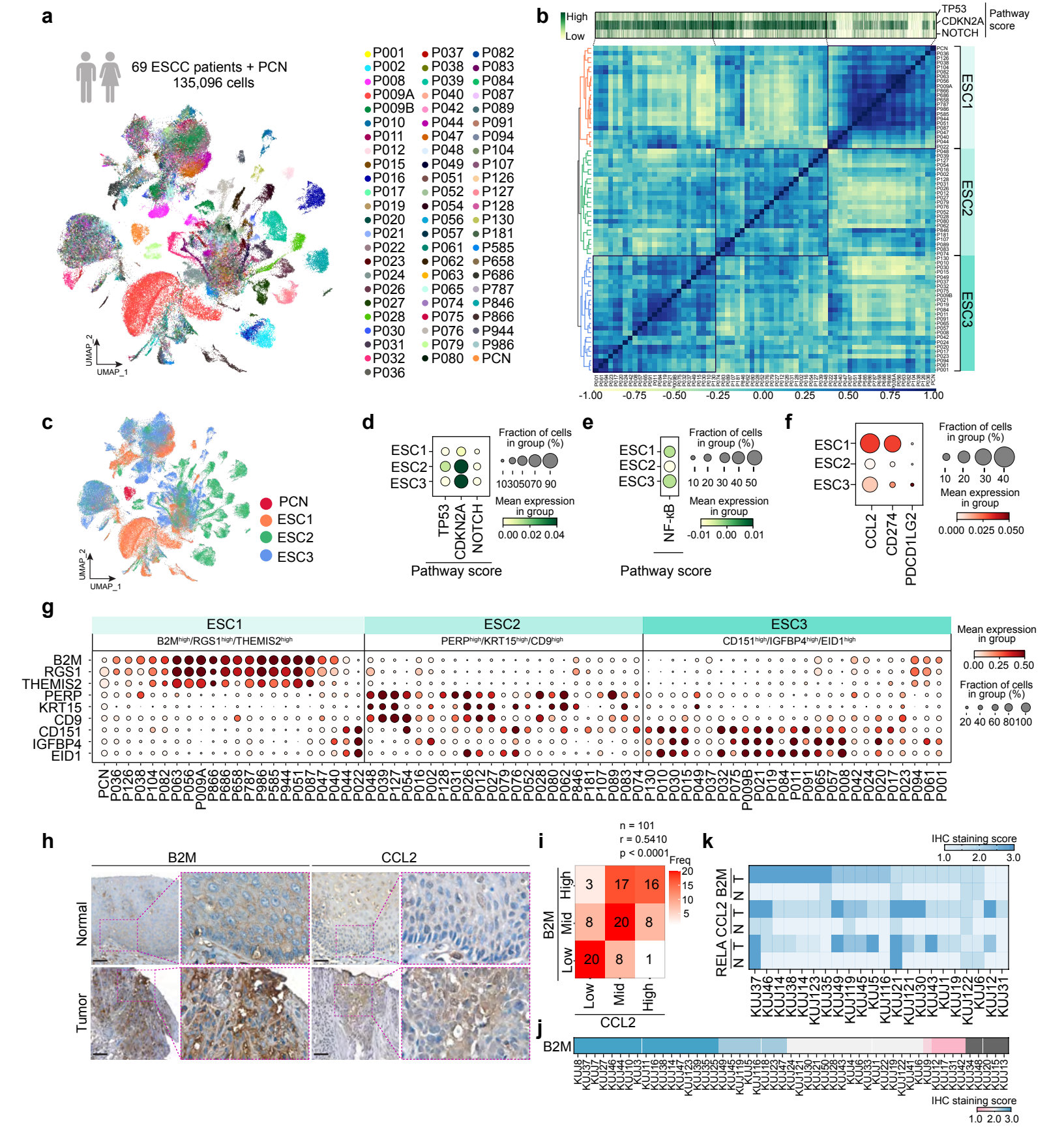
a
69 ESCC patients + PCN
135,096 cells
UMAP_2
UMAP_1
P001 P002 P008 P009A P009B P010 P011 P012 P015 P016 P017 P019 P020 P021 P022 P023 P024 P026 P027 P028 P030 P031 P032 P036
P037 P038 P039 P040 P042 P044 P047 P048 P049 P051 P052 P054 P056 P057 P061 P062 P063 P064 P065 P074 P075 P076 P079 P080
P082 P083 P084 P087 P089 P091 P094 P104 P107 P126 P127 P128 P130 P181 P585 P658 P686 P787 P846 P866 P944 P986 PCN
b
High
Low
TP53
CDKN2A
NOTCH
Pathway score
ESC1
ESC2
ESC3
-1.00 -0.75 -0.50 -0.25 0.00 0.25 0.50 0.75 1.00
c
PCN
ESC1
ESC2
ESC3
UMAP_2
UMAP_1
d
ESC1
ESC2
ESC3
TP53
CDKN2A
NOTCH
Pathway score
Fraction of cells in group (%)
10 30 50 70 90
Mean expression in group
0.00 0.02 0.04
e
ESC1
ESC2
ESC3
NF-κB
Pathway score
Fraction of cells in group (%)
10 20 30 40 50
Mean expression in group
-0.01 0.00 0.01
f
ESC1
ESC2
ESC3
CCL2
CD274
PDCD1LG2
Fraction of cells in group (%)
10 20 30 40
Mean expression in group
0.000 0.025 0.050
g
ESC1
B2M^high/RGS1^high/THEMIS2^high
ESC2
PERP^high/KRT15^high/CD9^high
ESC3
CD151^high/IGFBP4^high/EID1^high
B2M
RGS1
THEMIS2
PERP
KRT15
CD9
CD151
IGFBP4
EID1
PCN P036 P126 P038 P104 P082 P063 P056 P009A P866 P686 P658 P787 P986 P585 P944 P051 P087 P047 P040 P044 P022
P048 P039 P127 P054 P016 P002 P128 P031 P026 P012 P027 P079 P076 P052 P028 P080 P062 P846 P181 P107 P089 P083 P074
P130 P010 P030 P015 P049 P037 P032 P075 P009B P021 P019 P084 P011 P091 P065 P057 P008 P042 P024 P020 P017 P023 P094 P061 P001
Mean expression in group
0.00 0.25 0.50
Fraction of cells in group (%)
20 40 60 80 100
h
B2M
CCL2
Normal
Tumor
i
n = 101
r = 0.5410
p < 0.0001
Freq
20
15
10
5
B2M
High
Mid
Low
3 17 16
8 20 8
20 8 1
CCL2
Low
Mid
High
k
IHC staining score
1.0 2.0 3.0
B2M
CCL2
RELA
N T N T N T
KUJ37 KUJ46 KUJ14 KUJ38 KUJ14 KUJ123 KUJ35 KUJ49 KUJ119 KUJ45 KUJ5 KUJ116 KUJ21 KUJ121 KUJ30 KUJ43 KUJ1 KUJ19 KUJ122 KUJ6 KUJ12 KUJ31
j
B2M
KUJ8 KUJ37 KUJ27 KUJ46 KUJ14 KUJ13 KUJ11 KUJ16 KUJ38 KUJ14 KUJ47 KUJ123 KUJ39 KUJ35 KUJ25 KUJ49 KUJ45 KUJ119 KUJ5 KUJ18 KUJ23 KUJ47 KUJ24 KUJ121 KUJ30 KUJ21 KUJ50 KUJ28 KUJ43 KUJ4 KUJ46 KUJ33 KUJ21 KUJ19 KUJ122 KUJ41 KUJ6 KUJ9 KUJ12 KUJ17 KUJ31 KUJ42 KUJ34 KUJ48 KUJ20 KUJ13
IHC staining score
1.0 2.0 3.0
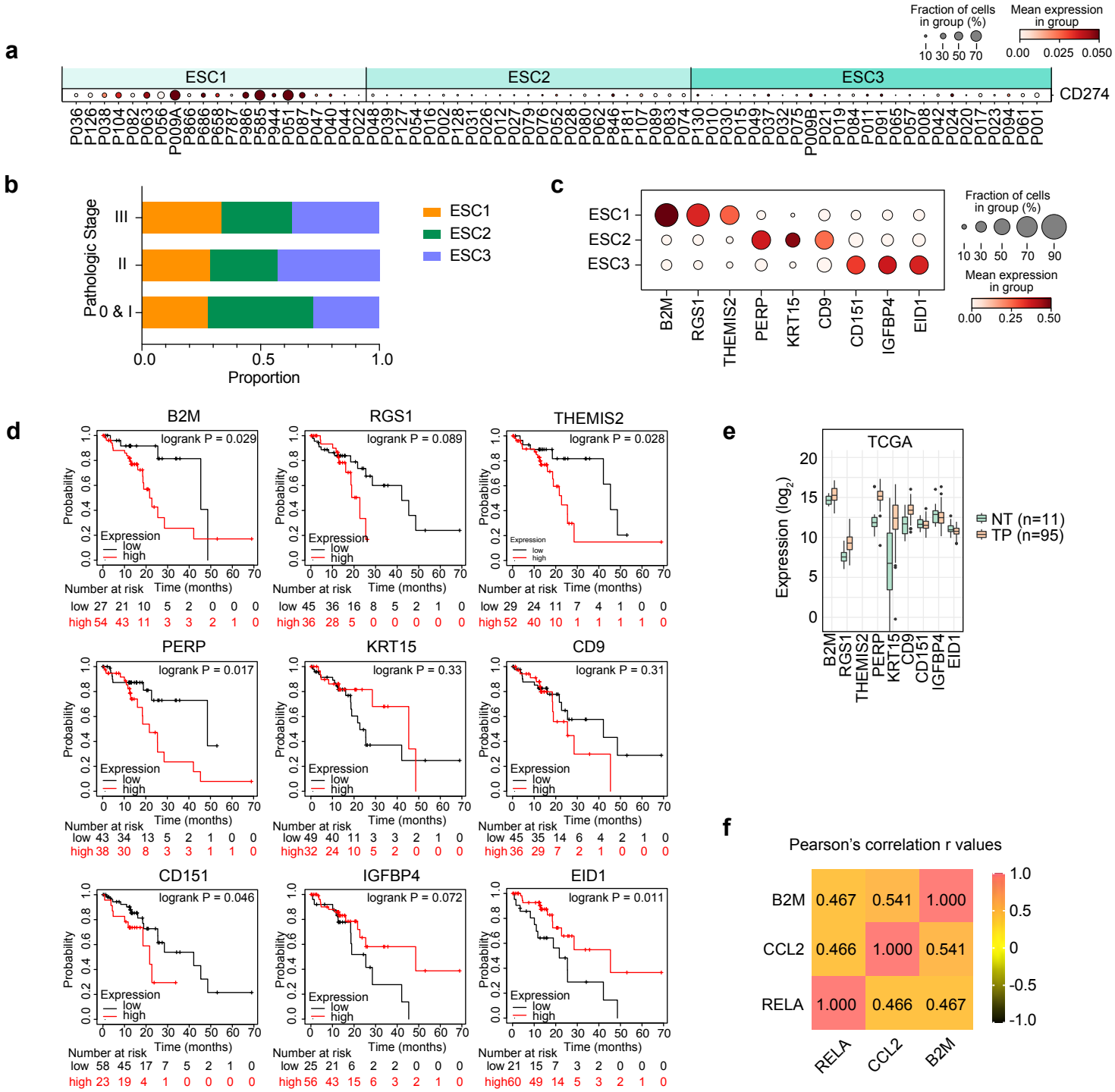
Extended Data 10